AIMS Mathematics, 10(7): 15165–15192.
DOI: 10.3934/math.2025680
Received: 22 November 2024
Revised: 05 February 2025
Accepted: 11 February 2025
Published: 01 July 2025

http://www.aimspress.com/journal/Math

Research article

Analysis of exceptional surfaces via Doppler- and Zeeman-affected non-Hermitian Hamiltonian in a three-level atomic system

Abdul Majeed[1], **Obaid J. Algahtani**[2], **Imdad Ullah**[1], **Amir Ali**[3,*] **and Dragan Pamucar**[4,5,6]

[1] Department of Physics, University of Malakand, Chakdara Dir(L), Khyber Pakhtunkhwa, Pakistan
[2] Department of Mathematics, College of Science, King Saud University, P. O. Box 2455, Riyadh 11451, Saudi Arabia
[3] Department of Mathematics, University of Malakand, Chakdara Dir(L), Khyber Pakhtunkhwa, Pakistan
[4] Department of Operations Research and Statistics, Faculty of Organizational Sciences, University of Belgrade, Belgrade, Serbia
[5] Department of Industrial Engineering & Management, Yuan Ze University, Taoyuan City 320315, Taiwan
[6] Department of Applied Mathematical Science, College of Science and Technology, Korea University, Sejong 30019, Republic of Korea

* **Correspondence:** Email: amiralishahs@yahoo.com, amirali@uom.edu.pk.

Abstract: The exceptional surface of the Doppler- and Zeeman-affected non-Hermitian Hamiltonian of a three-level atomic medium, driven by one probe and two control fields, was controlled and modified. Multiple exceptional surfaces of the second and third orders were reported based on the real part of eigenstates and the real and imaginary parts of the eigenvalues of the non-Hermitian Hamiltonian. The exceptional surfaces and degeneracy regions were studied with variations in detunings, Rabi frequencies, decay rates, phases, and Doppler and Zeeman widths. The effect of the Doppler shift was obtained by the average of $\lambda_i(kv)$ and $S_i(kv)$ over the Maxwellian distribution, while the Zeeman shift was obtained by the average of $\lambda_i(\mu B)$ and $S_i(\mu B)$ over the Gaussian distribution. The exceptional surfaces shift with both Zeeman and Doppler shift. The degeneracy increases with an increase in the Zeeman effect. With an increase in Doppler width, the degeneracy in the real part of the eigenvalues also increases but decreases in the imaginary part of eigenvalues. The maximum range of degeneracy of Zeeman-affected exceptional surfaces was investigated with decay rates and Rabi frequencies of the coupled driving fields, while for Doppler-affected exceptional surfaces, it was investigated with detuning and Rabi frequencies. The modified results of exceptional surfaces are useful for hybrid quantum systems, artificial intelligence, entanglement physics, quantum state sensing, and optics.

Keywords: exceptional surfaces; non-Hermitian Hamiltonian; Doppler and Zeeman effect; eigenstates; eigenvalues; three-level atomic system
Mathematics Subject Classification: 15A18, 45A05, 45C05, 70H05, 78A10, 81-10, 81Q93

1. Introduction

When two or more eigenvalues and eigenstates in a non-Hermitian system become identical, this is known as an exceptional point or surface. In contrast, a diabolic point occurs when the eigenvalues of a Hermitian system coincide [1], while for an exceptional point, both the eigenvalues and eigenvectors should coincide [2]. Doppler-affected exceptional points are found in systems where the Doppler effect modifies the parameters of a non-Hermitian Hamiltonian, changing the location and behavior of the exceptional point. Due to relative motion, the Doppler effect usually causes a shift in wave frequency. In non-Hermitian systems, this shift can alter the eigenvalue structure and degeneracy requirements related to exceptional points. Depending on how motion and non-Hermitian parameters interact, the system can be broken, changed, or restored. The Doppler shift can decrease the number of degenerate instances where the eigenvalues are the same by breaking the symmetry of the system. Multiple eigenvalues may come together as a result of system adjustments induced by the Doppler effect, increasing the system's degeneracy. Applying the Zeeman effect to a non Hermitian system can shift, modify, or create new exceptional points, with corresponding changes in system properties and behaviors.

Exceptional points occur when eigenvalues and eigenvectors coalesce, and the Zeeman shift modifies the Hamiltonian, potentially shifting, merging, or eliminating exceptional points. In the context of exceptional points, the Zeeman effect does not cause the typical splitting of energy levels; instead, in non-Hermitian systems, the Zeeman effect shifts the position of the exceptional point and increases degeneracy [3]. This means that more eigenvalues and eigenstates coalesce at the exceptional point, enhancing the system's sensitivity to external perturbations.

The concept of exceptional points was introduced in the mid-20th century as researchers studied non-Hermitian systems, which differ from traditional Hermitian operators in quantum mechanics. They were initially identified in the context of complex energy spectra in nuclear and atomic physics. Over time, the understanding of exceptional points grew, revealing their significance in the broader field of physics [4–6]. The concept of non-Hermitian exceptional points has applications in a wide range of disciplines such as laser enhancements [7], optical sensors [8], mode switching [9–11], nonreciprocal light propagation [12, 13], quantum phase transitions [14], quantum state sensing [15], enhanced plasmonic sensing [16], metamaterials [17], engineering [18, 19], tactile sensors and optical gyroscopes [20], optomechanics [21], thermal mapping [22, 23], quantum process tomography [24], optics [25], optical microcavities [8], electromagnetics [26], biological systems [27], photonics [28], optical sensors [29], sensing limitations at an exceptional point [30] and hybrid quantum systems [31]. A number of researchers have focused on exceptional points and surfaces utilizing different strategies and frameworks.

Goldzak et al. [32] studied light stops at exceptional points. Mandal et al. [33] examined higher-order exceptional points. Zhang [34] studied dynamically encircling exceptional points in a three-mode

waveguide system. Kawabata [35] performed two experiments on exceptional sensing and transport. Ramezanpour et al. [36] studied the tuning of exceptional points with Kerr nonlinearity. Brandstetter et al. [37] studied reversing the pump dependence of a laser at an exceptional point. Kodigala et al. [38] studied exceptional points in three-dimensional plasmonic nanostructures. Chen et al. [39] studied, revealing the missing dimension at an exceptional point. Zhang et al. [40] studied phonon laser operating at an exceptional point. Cwolf et al. [41] analysed the time evolution of shifting exceptional points. Even et al. [42] studied exceptional points in coupled pendulums by experimental observation. Bulgakov et al. [43] studied exceptional points in a dielectric spheroid.

Here, we investigate the coherent manipulation of exceptional surfaces in Doppler- and Zeeman-affected non-Hermitian hamiltonian in a three-level atomic medium. A three-level ladder-shaped atomic medium coupled with three driving fields is used to control and manipulate the exceptional surface by application of driving fields. The multiple exceptional surfaces are reported by real and imaginary parts of the eigenvalues. This modified work may close a huge gap in the high-tech application of photonics, hybrid quantum systems, optical gyroscopes, and thermal mappings.

2. Modeling and kinetics

Consider a three-level non-Hermitian ladder-shaped atomic system having one ground state, one excited state, and one super excited state as shown in Figure 1(a). Figure 1(b) shows the Doppler broadened system [44], and Figure 1(c) shows the Zeeman-affected system [3]. The ground state $|1\rangle$ and state $|2\rangle$ are coupled by a controlled field E_1 of Rabi frequency σ_1 with detuning Δ_1 and γ_{21} showing particle decay from state $|2\rangle$ to ground state $|1\rangle$. The states $|2\rangle$ and $|3\rangle$ are coupled by a controlled field E_2 of Rabi frequency σ_2 with detuning Δ_2 and γ_{32} showing particle decay from state $|3\rangle$ to ground state $|2\rangle$. The ground state $|1\rangle$ and state $|3\rangle$ are coupled by a probe field E_p of Rabi frequency σ_P with detuning Δ_P. The experimental setup [45] of exceptional points is shown in Figure 2.

The Doppler-affected Hamiltonian for a three-level atomic system is written as

$$\begin{aligned} H &= \hbar\Big[(\Delta_1 + i\gamma_{21} + \eta_1 k_1 v)|2\rangle\langle 2| + (\Delta_2 + i\gamma_{31} + \eta_2 k_2 v)|3\rangle\langle 3| + \sigma_1|1\rangle\langle 2| + \sigma_1^*|2\rangle\langle 1| \\ &\quad +\sigma_p|1\rangle\langle 3| + \sigma_p^*|3\rangle\langle 1| + \sigma_2|2\rangle\langle 3| + \sigma_2^*|3\rangle\langle 2|\Big]. \end{aligned} \tag{2.1}$$

The Doppler-affected Hamiltonian matrix is described as

$$H = \begin{pmatrix} 0 & \sigma_1 & \sigma_P \\ \sigma_1^* & E & \sigma_2 \\ \sigma_P^* & \sigma_2^* & F \end{pmatrix}. \tag{2.2}$$

The Doppler-affected eigenvalues of non-Hermitian Hamiltonian are calculated by using the secular equation $|H - \lambda I| = 0$ as

$$\lambda_1(kv) = \frac{a_1}{3} + \frac{2^{1/3}(-a_1^2 - 3a_2)}{3Q} - \frac{Q}{3\cdot 2^{1/3}}, \tag{2.3}$$

$$\lambda_2(kv) = \frac{a_1}{3} - \frac{(1 + i\sqrt{3})(-a_1^2 - 3a_2)}{3\cdot 2^{2/3}Q} + \frac{(1 - i\sqrt{3})Q}{6\cdot 2^{1/3}}, \tag{2.4}$$

$$\lambda_3(kv) = \frac{a_1}{3} - \frac{(1 - i\sqrt{3})(-a_1^2 - 3a_2)}{3\cdot 2^{2/3}Q} + \frac{(1 + i\sqrt{3})Q}{6\cdot 2^{1/3}}. \tag{2.5}$$

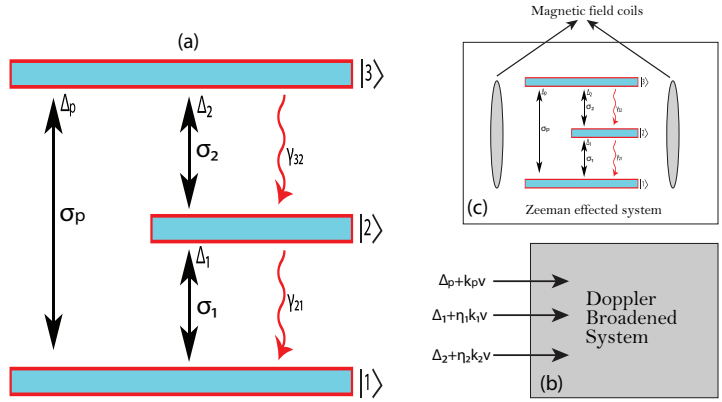

Figure 1. (a) Three-level ladder-shaped non-Hermitian medium. (b) Doppler broadened system [44]. (c) Zeeman-affected system [3].

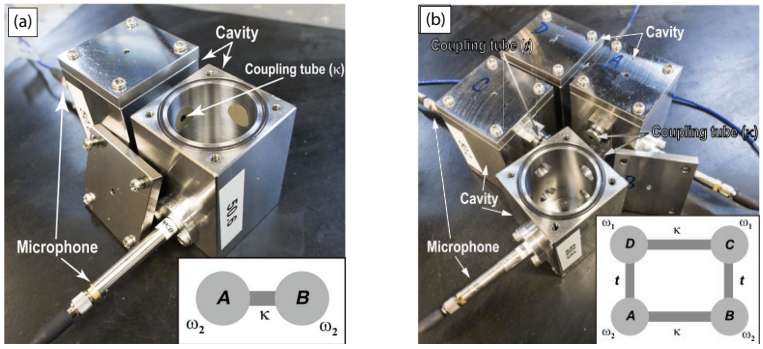

Figure 2. The experimental setup of exceptional points [45].

The Doppler-affected eigenstates of non-Hermitian Hamiltonian is described as

$$S_1(kv) = \frac{1}{\sqrt{3}}\left(\alpha_{1D}e^{\frac{-i\lambda_1(kv)t}{\hbar}} + \beta_{1D}e^{\frac{-i\lambda_2(kv)t}{\hbar}} + \gamma_{1D}e^{\frac{-i\lambda_3(kv)t}{\hbar}}\right), \tag{2.6}$$

$$S_2(kv) = \frac{1}{\sqrt{3}}\left(\alpha_{2D}e^{\frac{-i\lambda_1(kv)t}{\hbar}} + \beta_{2D}e^{\frac{-i\lambda_2(kv)t}{\hbar}} + \gamma_{2D}e^{\frac{-i\lambda_3(kv)t}{\hbar}}\right), \tag{2.7}$$

$$S_3(kv) = \frac{1}{\sqrt{3}}\left(\alpha_{3D}e^{\frac{-i\lambda_1(kv)t}{\hbar}} + \beta_{3D}e^{\frac{-i\lambda_2(kv)t}{\hbar}} + \gamma_{3D}e^{\frac{-i\lambda_3(kv)t}{\hbar}}\right). \tag{2.8}$$

The Doppler affect for the three-level Hamiltonian is incorporated through the Maxwellian distribution by integrating the term ηkv, where η represents the direction of the applied field and v is the velocity of the medium. This inclusion accounts for the velocity-dependent frequency shift experienced by the atomic transitions due to the motion of the medium, effectively modifying the detuning terms in the Hamiltonian. The effect of the Doppler shift for the eigenvalue is the average of $\lambda_i(kv)$ over the Maxwellian distribution and is described as

$$\lambda_i = \frac{1}{V_D\sqrt{\pi}}\int_{-\infty}^{\infty}\lambda_i(kv)e^{-\frac{(kv)^2}{V_D^2}}d(kv). \tag{2.9}$$

The effect of the Doppler shift for the eigenstate is the average of $S_i(kv)$ over the Maxwellian distribution and is described as

$$S_i = \frac{1}{V_D\sqrt{\pi}}\int_{-\infty}^{\infty}S_i(kv)e^{-\frac{(kv)^2}{V_D^2}}d(kv), \tag{2.10}$$

where V_D is the Doppler width and depends on the absolute temperature. Its value is written as $V_D = \sqrt{K_B T \omega_p^2 / Mc^2}$, where ω_p is the frequency of probe field, K_B is the Boltzmann constant, T is the absolute temperature, M is the molecular mass, and c is the speed of light in vacuum. The supposition in the above matrix and the equations of the Doppler system are

$$E = \Delta_1 + \eta_1 k_1 v + i\gamma_{21}, \tag{2.11}$$

$$F = \Delta_2 + \eta_2 k_2 v + i\gamma_{32}, \tag{2.12}$$

$$a_1 = E + F, \tag{2.13}$$

$$a_2 = \sigma_1^2 + \sigma_2^2 + \sigma_p^2 - EF, \tag{2.14}$$

$$a_3 = \sigma_1 \sigma_2 \sigma_p^* + \sigma_p \sigma_1^* \sigma_2^* - E\sigma_p^2 - F\sigma_1^2, \tag{2.15}$$

$$Q = \left(-2a_1^3 - 9a_1 a_2 - 27a_3 + 3\sqrt{3}\sqrt{-a_1^2 a_2^2 - 4a_2^3 + 4a_1^3 a_3 + 18a_1 a_2 a_3 + 27a_3^2}\right)^{1/3}, \tag{2.16}$$

$$\alpha_{1D} = \frac{\sigma_1 \beta_{11} + \sigma_p}{\lambda_1(kv)}, \tag{2.17}$$

$$\beta_{1D} = \frac{\left(\sigma_1^* \sigma_p\right)/\lambda_1(kv) + \sigma_2}{\left(\sigma_1^2\right)/\lambda_1(kv) + E - \lambda_1(kv)}, \tag{2.18}$$

$$\alpha_{2D} = \frac{\sigma_1 \beta_{22} + \sigma_p}{\lambda_2(kv)}, \tag{2.19}$$

$$\beta_{2D} = \frac{\left(\sigma_1^* \sigma_p\right)/\lambda_2(kv) + \sigma_2}{\left(\sigma_1^2\right)/\lambda_2(kv) + E - \lambda_2(kv)}, \tag{2.20}$$

$$\alpha_{3D} = \frac{\sigma_1 \beta_{33} + \sigma_p}{\lambda_3(kv)}, \tag{2.21}$$

$$\beta_{3D} = \frac{\left(\sigma_1^* \sigma_p\right)/\lambda_3(kv) + \sigma_2}{\left(\sigma_1^2\right)/\lambda_3(kv) + E - \lambda_3(kv)}, \tag{2.22}$$

where $\gamma_{1D} = \gamma_{2D} = \gamma_{3D} = 1$. Now, the Zeeman-affected non-Hermitian Hamiltonian can be written as

$$\begin{aligned} H = {} & (\Delta_1 + \mu B + i\gamma_{21})|2\rangle\langle 2| + (\Delta_2 + \mu B + i\gamma_{31})|3\rangle\langle 3| + \sigma_1|1\rangle\langle 2| + \sigma_1^*|2\rangle\langle 1| + \sigma_p|1\rangle\langle 3| \\ & + \sigma_p^*|3\rangle\langle 1| + \sigma_2|2\rangle\langle 3| + \sigma_2^*|3\rangle\langle 2|. \end{aligned} \tag{2.23}$$

The Zeeman-affected Hamiltonian matrix is given as

$$H = \begin{pmatrix} 0 & \sigma_1 & \sigma_P \\ \sigma_1^* & A & \sigma_2 \\ \sigma_P^* & \sigma_2^* & B \end{pmatrix}. \tag{2.24}$$

The eigenvalues of Zeeman-affected non-Hermitian Hamiltonian are given as

$$\lambda_1(\mu B) = \frac{b}{3} + \frac{2^{1/3}(-b^2 - 3c)}{3S} - \frac{S}{3 \cdot 2^{1/3}}, \tag{2.25}$$

$$\lambda_2(\mu B) = \frac{b}{3} - \frac{(1 + i\sqrt{3})(-b^2 - 3c)}{3 \cdot 2^{2/3} S} + \frac{(1 - i\sqrt{3})S}{6 \cdot 2^{1/3}}, \tag{2.26}$$

$$\lambda_3(\mu B) = \frac{b}{3} - \frac{(1 - i\sqrt{3})(-b^2 - 3c)}{3 \cdot 2^{2/3} S} + \frac{(1 + i\sqrt{3})S}{6 \cdot 2^{1/3}}. \tag{2.27}$$

The Zeeman-affected eigenstates of non-Hermitian Hamiltonian are described as

$$S_1(\mu B) = \frac{1}{\sqrt{3}} \left(\alpha_{1Z} e^{\frac{-i\lambda_1(\mu B)t}{\hbar}} + \beta_{1Z} e^{\frac{-i\lambda_2(\mu B)t}{\hbar}} + \gamma_{1Z} e^{\frac{-i\lambda_3(\mu B)t}{\hbar}} \right), \tag{2.28}$$

$$S_2(\mu B) = \frac{1}{\sqrt{3}} \left(\alpha_{2Z} e^{\frac{-i\lambda_1(\mu B)t}{\hbar}} + \beta_{2Z} e^{\frac{-i\lambda_2(\mu B)t}{\hbar}} + \gamma_{2Z} e^{\frac{-i\lambda_3(\mu B)t}{\hbar}} \right), \tag{2.29}$$

$$S_3(\mu B) = \frac{1}{\sqrt{3}} \left(\alpha_{3Z} e^{\frac{-i\lambda_1(\mu B)t}{\hbar}} + \beta_{3Z} e^{\frac{-i\lambda_2(\mu B)t}{\hbar}} + \gamma_{3Z} e^{\frac{-i\lambda_3(\mu B)t}{\hbar}} \right). \tag{2.30}$$

The Zeeman effect is incorporated into the non-Hermitian Hamiltonian through Gaussian distribution, where the integration is carried out over the term μB. Here, μ represents the magnetic dipole moment, and B is the external magnetic field. The effect of the Zeeman shift of eigenvalues is the average of $\lambda_i(\mu B)$ over the Gaussian distribution and is described as

$$\lambda_i = \frac{1}{W_z \sqrt{2\pi}} \int_{-\infty}^{\infty} \lambda_i(\mu B) e^{-\frac{(\mu B)^2}{W_z^2}} d(\mu B). \tag{2.31}$$

The effect of the Zeeman shift of the eigenstate is the average of $S_i(\mu B)$ over the Gaussian distribution and is described as

$$S_i = \frac{1}{W_z \sqrt{2\pi}} \int_{-\infty}^{\infty} S_i(\mu B) e^{-\frac{(\mu B)^2}{W_z^2}} d(\mu B), \tag{2.32}$$

where W_z is the Zeeman width and is associated with the spread of the distribution around its mean. The supposition in the Zeeman system is

$$A = \Delta_1 + \mu B + i\gamma_{21}, \tag{2.33}$$

$$B = \Delta_2 + \mu B + i\gamma_{32}, \tag{2.34}$$

$$b = A + B, \tag{2.35}$$

$$c = \sigma_1^2 + \sigma_2^2 + \sigma_p^2 - AB, \tag{2.36}$$

$$d = \sigma_1 \sigma_2 \sigma_p^* + \sigma_p \sigma_1^* \sigma_2^* - A\sigma_p^2 - B\sigma_1^2, \tag{2.37}$$

$$S = \left(-2b^3 - 9bc - 27d + 3\sqrt{3}\sqrt{-b^2c^2 - 4c^3 + 4b^3d + 18bcd + 27d^2} \right)^{1/3}, \tag{2.38}$$

$$\alpha_{1Z} = \frac{\sigma_1 \beta_{11} + \sigma_p}{\lambda_1(\mu B)}, \tag{2.39}$$

$$\beta_{1Z} = \frac{\left(\sigma_1^* \sigma_p\right)/\lambda_1(\mu B) + \sigma_2}{\left(\sigma_1^2\right)/\lambda_1(\mu B) + A - \lambda_1(\mu B)}, \tag{2.40}$$

$$\alpha_{2Z} = \frac{\sigma_1 \beta_{22} + \sigma_p}{\lambda_2(\mu B)}, \tag{2.41}$$

$$\beta_{2Z} = \frac{\left(\sigma_1^*\sigma_p\right)/\lambda_2(\mu B) + \sigma_2}{\left(\sigma_1^2\right)/\lambda_2(\mu B) + A - \lambda_2(\mu B)}, \tag{2.42}$$

$$\alpha_{3Z} = \frac{\sigma_1\beta_{33} + \sigma_p}{\lambda_3(\mu B)}, \tag{2.43}$$

$$\beta_{3Z} = \frac{\left(\sigma_1^*\sigma_p\right)/\lambda_3(\mu B) + \sigma_2}{\left(\sigma_1^2\right)/\lambda_3(\mu B) + A - \lambda_3(\mu B)}, \tag{2.44}$$

where $\gamma_{1Z} = \gamma_{2Z} = \gamma_{3Z} = 1$. Here, σ_j and σ_j^* are

$$\sigma_j = |\sigma_j| \exp[\iota\psi_j], \tag{2.45}$$

$$\sigma_j^* = |\sigma_j| \exp[-\iota\psi_j], \tag{2.46}$$

where j=1, 2, p.

3. Results and discussion

The results are presented for exceptional surfaces of non-Hermitian Hamiltonian for three cases: in the absence of any shift, in the presence of the Doppler shift, and in the presence of the Zeeman shift in a three-level atomic medium. The decay rate is taken as $\gamma = 1GHz$, and other parameters are scaled to this decay rate γ. Here, the Doppler width is taken as $V_D = 16\gamma$, and the Zeeman width is $W_z = 20\gamma$. The red, green, and blue surfaces represent the first, second, and third eigenvalues or eigenstates of the non-Hermitian Hamiltonian, respectively.

3.1. In the absence of shifts

In this section, plots are displayed for the real and imaginary parts of eigenvalues λ_i and the real part of eigenstates $S_i(t)$ versus Rabi frequency $\sigma_{1,2,p}$, detuning $\Delta_{1,p}$, decay rate γ_{32}, and phases $\psi_{1,p}$ in the absence of any shift.

Figure 3 shows the real and imaginary parts of eigenvalues of λ_i, where $i = 1, 2, 3$, versus mode of Rabi frequency $|\sigma_2|/\gamma$ and probe field detuning Δ_p/γ. The imaginary parts of three eigenvalues of non-Hermitian Hamiltonian coincide at the resonance surface $|\sigma_2| = 1.9\gamma$. This is a third-order exceptional surface, and the exceptional surface values are 0 and $|\sigma_2| = 1.9\gamma$. The three eigenvalues show degeneracy in the range of $0\gamma \leq |\sigma_2| \leq 1.9\gamma$ and $-10\gamma \leq \Delta_p \leq 10\gamma$, as illustrated in Figure 3. The real part of λ_i shows one third-order and two second-order exceptional surfaces. The three eigenvalues λ_i coincide at resonance surface $|\sigma_2| = 5\gamma$, and exceptional surface values are 0 and $|\sigma_2| = 5\gamma$, showing degeneracy in the range of $-10\gamma \leq \Delta_p \leq 10\gamma$ and $5\gamma \leq |\sigma_2| \leq 20\gamma$. The two eigenvalues λ_2 and λ_3 coincide at the resonance surface $|\sigma_2| = 1.9\gamma$, and exceptional surface values are 0.5 and $|\sigma_2| = 1.9\gamma$, showing degeneracy in the range of $-10\gamma \leq \Delta_p \leq 10\gamma$. The two eigenvalues λ_1 and λ_2 coincide at resonant point $|\sigma_2| = 1.9\gamma$, and exceptional surface values are -0.5 and $|\sigma_2| = 1.9\gamma$, showing degeneracy in the range of $-10\gamma \leq \Delta_p \leq 10\gamma$, as illustrated in Figure 3. The same plot for the Doppler-affected eigenvalues is shown in Figure 9, while the plot for Zeeman-affected eigenvalues is illustrated in Figure 19.

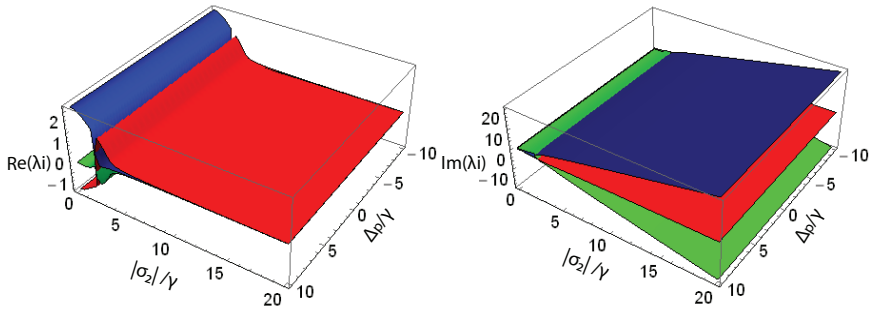

Figure 3. The real and imaginary parts of eigenvalues versus Rabi frequency σ_2 and detuning Δ_p. Other parameters values are, $\gamma_{21} = 0.89\gamma$, $\gamma_{32} = 0.98\gamma$, $\Delta_1 = -0.5\gamma$, $\Delta_2 = 0.5\gamma$, $|\sigma_p| = 2\gamma$, $|\sigma_1| = 0.5\gamma$, $\psi_p = 2\pi$, $\psi_1 = \pi$, and $\psi_2 = \pi/2$.

Figure 4 displays the real and imaginary parts of eigenvalues of λ_i, where $i = 1, 2, 3$, versus mode of Rabi frequency $|\sigma_1|/\gamma$ and phase angle ψ_p. The imaginary parts of three eigenvalues of a non-Hermitian Hamiltonian coincide at the resonance surface $|\sigma_1| = 9\gamma$. This is a third-order exceptional surface of a non-Hermitian Hamiltonian in a three-level atomic medium, and the exceptional surface values are 0 and $|\sigma_1| = 9\gamma$. The three eigenvalues show degeneracy in the range of $0\gamma \leq |\sigma_1| \leq 9\gamma$ and $0 \leq \psi_p \leq 2\pi$, as illustrated in Figure 4. The real part of λ_i shows one third-order and three second-order exceptional surfaces. The three eigenvalues of a non-Hermitian Hamiltonian coincide at point $|\sigma_1| = 4\gamma$. This is a third-order exceptional surface of a non-Hermitian Hamiltonian in a three-level atomic medium, and the exceptional surface values are 0 and $|\sigma_1| = 4\gamma$ and show degeneracy in the range of $0\gamma \leq |\sigma_1| \leq 4\gamma$ and $0 \leq \psi_p \leq 2\pi$. The two eigenvalues λ_2 and λ_3 coincide at resonance surface $|\sigma_1| = 14\gamma$, and the exceptional surface values are -10 and $|\sigma_1| = 14\gamma$, showing degeneracy in the range of $14\gamma \leq |\sigma_1| \leq 20\gamma$ and $0 \leq \psi_p \leq 2\pi$. The two eigenvalues λ_2 and λ_3 again coincide at two resonance surfaces $|\sigma_1| = 7\gamma$ and $|\sigma_1| = 3\gamma$, and exceptional surface values are -5 and $|\sigma_1| = 7\gamma$, and -1 and $|\sigma_1| = 3\gamma$, showing degeneracy in the range of $0 \leq \psi_p \leq 2\pi$, as illustrated in Figure 4. The same plot for Doppler-affected eigenvalues is illustrated in Figure 10, while the plot for Zeeman-affected eigenvalues is illustrated in Figure 20.

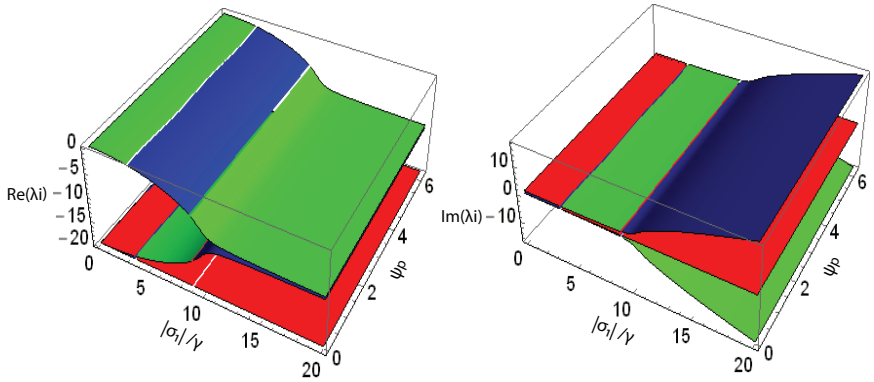

Figure 4. The real and imaginary parts of eigenvalues versus Rabi frequency σ_1 and phase ψ_p. Other parameters values are, $\gamma_{21} = 0.9\gamma$, $\gamma_{32} = 0.08\gamma$, $\Delta_1 = -20\gamma$, $\Delta_2 = -20\gamma$, $\Delta_p = 20\gamma$, $|\sigma_p| = 0.1\gamma$, $|\sigma_2| = 10^{-}19\gamma$, $\psi_1 = 0.5\pi$, and $\psi_2 = 0.4\pi$.

Figure 5 displays for real and imaginary parts of eigenvalues of λ_i, where $i = 1, 2, 3$, versus mod of Rabi frequency $|\sigma_p|/\gamma$ and decay rate γ_{21}. The imaginary part shows one third-order and two second-order exceptional surfaces. The imaginary part of three eigenvalues of non-Hermitian Hamiltonian coincides at the resonance surface $|\sigma_p| = 9\gamma$. This is a third-order exceptional surface of a non-Hermitian Hamiltonian in a three-level atomic medium, and the exceptional surface values are 0 and $|\sigma_p| = 9\gamma$. The three eigenvalues show degeneracy in the range of $0\gamma \leq |\sigma_p| \leq 9\gamma$ and $0 \leq \gamma_{21} \leq 2$. The two eigenvalues λ_2 and λ_3 coincide at resonance surface $|\sigma_p| = 18\gamma$, and exceptional surface values are 4 and $|\sigma_p| = 18\gamma$. The other two eigenvalues λ_1 and λ_1 coincide at resonance surface $|\sigma_p| = 20\gamma$, and exceptional surface values are -4 and $|\sigma_p| = 20\gamma$, as illustrated in Figure 5. The real part of λ_i shows five second-order exceptional surfaces. The two eigenvalues λ_2 and λ_3 coincide at three resonance surfaces $|\sigma_p| = 4\gamma$, $|\sigma_p| = 12\gamma$, and $|\sigma_p| = 22\gamma$, and exceptional surface values are 6 and $|\sigma_p| = 4\gamma$ and 3 and $|\sigma_p| = 12\gamma$, and others are -5 and $|\sigma_p| = 22\gamma$, which show degeneracy in the range of $22\gamma \leq |\sigma_p| \leq 30\gamma$ and $0 \leq \gamma_{21} \leq 2$. The two eigenvalues λ_1 and λ_3 coincide at resonance surface $|\sigma_p| = 19\gamma$, and exceptional surface values are 2 and $|\sigma_p| = 19\gamma$. The other two eigenvalues λ_1 and λ_2 coincide at resonance surface $|\sigma_p| = 18\gamma$, and exceptional surface values are -5 and $|\sigma_p| = 18\gamma$, as illustrated in Figure 5.

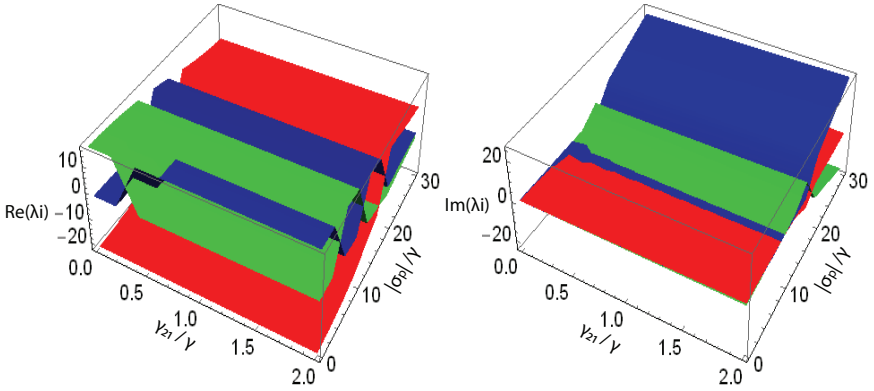

Figure 5. The real and imaginary parts of eigenvalues versus Rabi frequency σ_p and decay rate γ_{21}. Other parameters values are, $\gamma_{32} = 0.1\gamma$, $\Delta_1 = -2.5\gamma$, $\Delta_2 = -4.5\gamma$, $\Delta_p = -1.5\gamma$, $|\sigma_1| = 12\gamma$, $|\sigma_2| = 15\gamma$, $\psi_1 = \pi/2$, $\psi_1 = \pi$, $\psi_2 = \pi$.

Figure 6 displays for real and imaginary parts of eigenvalues of λ_i, where $i = 1, 2, 3$, versus the mod of Rabi frequency $|\sigma_p|/\gamma$ and decay rate γ_{32}/γ. The imaginary parts of three eigenvalues of non-Hermitian Hamiltonian coincide at the resonance surface $|\sigma_p| = 10\gamma$; this is a third-order exceptional surface of non-Hermitian Hamiltonian in a three-level atomic medium, and the exceptional surface values are 0 and $|\sigma_p| = 10\gamma$. The three eigenvalues show degeneracy in the range of $0\gamma \leq |\sigma_p| \leq 10\gamma$ and $0\gamma \leq \gamma_{32} \leq 1\gamma$, as illustrated in Figure 6. The real part of λ_i shows two second-order exceptional surfaces. The two eigenvalues λ_2 and λ_3 coincide at resonance surface $|\sigma_p| = 10\gamma$, and exceptional surface values are 10 and $|\sigma_p| = 10\gamma$, showing degeneracy in the range of $10\gamma \leq |\sigma_p| \leq 30\gamma$ and $0\gamma \leq \gamma_{32} \leq 1\gamma$. The two eigenvalues λ_1 and λ_2 coincide at resonance surface $|\sigma_p| = 2\gamma$ and exceptional surface values are 0 and $|\sigma_p| = 2\gamma$, showing degeneracy in the range of $0\gamma \leq |\sigma_p| \leq 2\gamma$ and $0\gamma \leq \gamma_{32} \leq 1\gamma$, as illustrated in Figure 6.

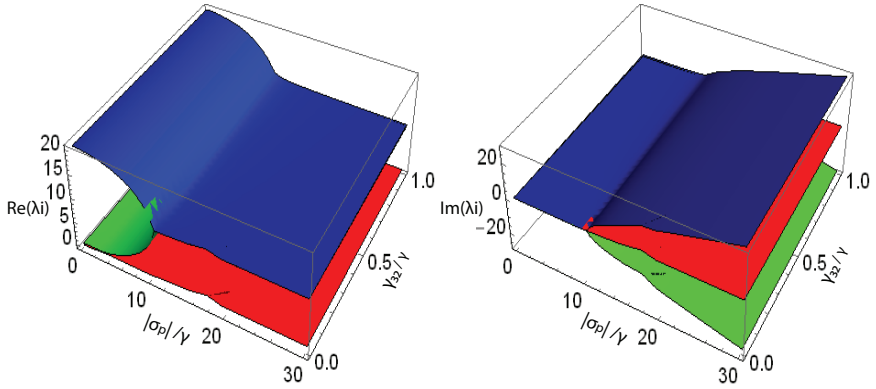

Figure 6. The real and imaginary parts of eigenvalues versus Rabi frequency σ_p and decay rate γ_{32}. Other parameters values are, $\gamma_{21} = 0.001\gamma$, $\Delta_1 = 0.0001\gamma$, $\Delta_2 = 20\gamma$, $\Delta_p = 2\gamma$, $|\sigma_1| = 0.02\gamma$, $|\sigma_2| = 3\gamma$, $\psi_1 = \pi/10$,$\psi_2 = 2\pi/2$, and $\psi_p = \pi/2$.

In Figure 7, plots demonstrate the real part of eigenstate $S_i(t)$, where $i = 1, 2, 3$, against Rabi frequencies $\sigma_{p,2}/\gamma$ and normalized time t/τ. Figure 7(a) shows the real part of eigenstate against Rabi frequency σ_p/γ and time t/τ. The eigenstate is the function of Rabi frequency σ_p and time coordinate t/τ. The three eigenstates show degeneracy, which increases along Rabi frequency σ_p. The three eigenstates of $S_i(t)$ coincide at $\sigma_p = 3\gamma$, where the exceptional surface values are 0 and $\sigma_p = 3\gamma$. The three eigenstates of three-level non-Hermitian Hamiltonian show degeneracy in the region enclosed by the range $3\gamma \leq |\sigma_p| \leq 5\gamma$ and $0\tau \leq |t| \leq 5\tau$. The exceptional surfaces are controlled at Rabi frequencies $\sigma_1 = 15\gamma$, $\sigma_2 = 0.2\gamma$, detuning $\Delta_1 = 8\gamma$, $\Delta_{2,p} = 0\gamma$, decay rates, $\gamma_{21,32} = 0.1\gamma$, and phases $\psi_{1,2,p} = 0$. Figure 7(b) shows the real part of the eigenstate against Rabi frequency σ_2/γ and time t/τ. The eigenstate is the function of Rabi frequency σ_2 and time coordinate t/τ. The exceptional surfaces are controlled at Rabi frequencies $\sigma_p = 0.1\gamma$, $\sigma_1 = 5\gamma$, detuning $\Delta_p = 0.002\gamma$, $\Delta_{1,2} = 0\gamma$, decay rates, $\gamma_{21,32} = 0.001\gamma$ and phases, $\psi_{1,2,p} = 0$. The three eigenstates of $S_i(t)$ coincide at $\sigma_2 = 4\gamma$, where the exceptional surface values are 0 and $\sigma_2 = 4\gamma$. The three eigenstates of three-level non-Hermitian Hamiltonian show degeneracy in region enclosed by the range $3.5\gamma \leq |\sigma_2| \leq 4\gamma$ and $0\tau \leq |t| \leq 4\tau$. The same plot for the Doppler-affected eigenstate is shown in Figure 12, while the plot for Zeeman-affected eigenvalues is shown in Figure 23.

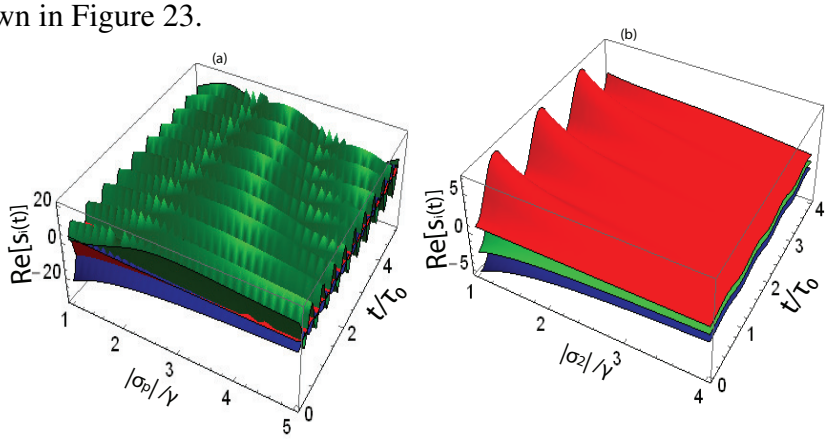

Figure 7. The real part of eigenstate versus Rabi frequency $\sigma_{p,2}$ and time t/τ. Other parameters values are, (a). $\sigma_1 = 15\gamma$, $\sigma_2 = 0.2\gamma$, $\Delta_1 = 8\gamma$, $\Delta_{2,p} = 0\gamma$, $\gamma_{21,32} = 0.1\gamma$, $\psi_{1,2,p} = 0$, (b). $\sigma_p = 0.1\gamma$, $\sigma_1 = 5\gamma$, $\Delta_1 = 0.002\gamma$, $\Delta_{1,2} = 0\gamma$, $\gamma_{21,32} = 0.001\gamma$, $\psi_{1,2,p} = 0$.

In Figure 8, plots demonstrate the real part of eigenstate $S_i(t)$, where $i = 1, 2, 3$, against Rabi frequency σ_1/γ, detuning Δ_2/γ, and normalized time t/τ. Figure 8(a) shows the real part of eigenstate against Rabi frequency σ_1/γ and time t/τ. The eigenstate is the function of Rabi frequency σ_1 and time coordinate t/τ. The three eigenstates show degeneracy, which decreases along Rabi frequency σ_1 and time coordinate. The three eigenstates of $S_i(t)$ coincide at $\sigma_1 = 1\gamma$, where the exceptional surface values are 0 and $\sigma_1 = 1\gamma$. The three eigenstates of three-level non-Hermitian Hamiltonian show degeneracy in the region enclosed by the range $0\gamma \leq |\sigma_1| \leq 3\gamma$ and $0\tau \leq |t| \leq 4\tau$. The exceptional surfaces are controlled at Rabi frequencies $\sigma_p = 0.1\gamma$, $\sigma_2 = 0.2\gamma$, detuning $\Delta_{1,2,3} = 0\gamma$, decay rates, $\gamma_{21} = 0.4\gamma$, $\gamma_{32} = 0.3\gamma$ and phases, $\psi_{1,2,p} = 0$. Figure 8(b) shows the real part of eigenstate against the control field detuning Δ_2/γ and time t/τ. The eigenstate is the function of detuning Δ_2 and time coordinate t/τ. The exceptional surfaces are controlled at Rabi frequencies $\sigma_{1,,2,p} = 0.01\gamma$, detuning $\Delta_1 = 0.1\gamma$, $\Delta_p = 2\gamma$, decay rates, $\gamma_{21} = 0.8\gamma$, $\gamma_{32} = 0.9\gamma$ and phases, $\psi_{1,2,p} = 0$. The three eigenstates of $S_i(t)$ coincide at $\Delta_2 = 1\gamma$, where the exceptional surface values are 0 and $\Delta_2 = 1\gamma$. The three eigenstates of three-level non-Hermitian Hamiltonian show degeneracy in the range of $1\gamma \leq |\Delta_2| \leq 4\gamma$, which decrease along the time coordinate t/τ. The same plot for the Doppler-affected eigenstate is shown in Figure 13, while the plot for Zeeman-affected eigenstate is shown in Figure 24.

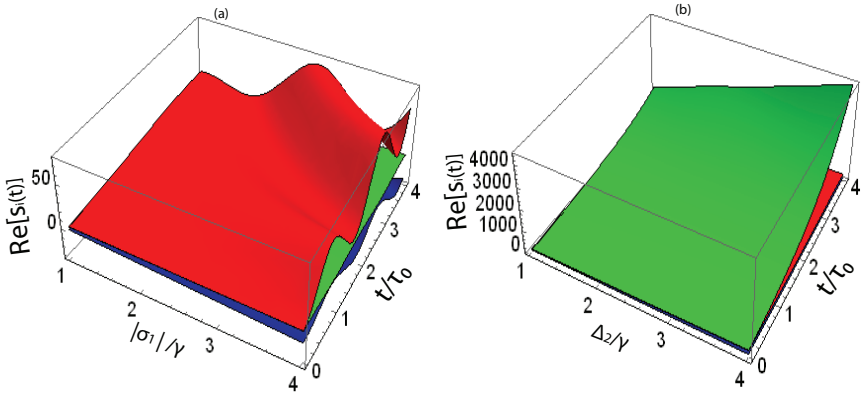

Figure 8. The real part of the eigenstate versus Rabi frequency σ_1, detuning Δ_2/γ and time t/τ. Other parameter values are (a) $\sigma_1 = 15\gamma$, $\sigma_2 = 0.2\gamma$, $\Delta_1 = 8\gamma$, $\Delta_{2,p} = 0\gamma$, $\gamma_{21,32} = 0.1\gamma$, $\psi_{1,2,p} = 0$, (b). $\sigma_p = 0.1\gamma$, $\sigma_1 = 5\gamma$, $\Delta_1 = 0.002\gamma$, $\Delta_{1,2} = 0\gamma$, $\gamma_{21,32} = 0.001\gamma$, $\psi_{1,2,p} = 0$.

3.2. In the presence of the Doppler shift

In this section, plots are displayed for the real and imaginary parts of eigenvalues and the real part of eigenstates versus Rabi frequency $\sigma_{1,2,p}$, detuning $\Delta_{1,p}$, decay rate γ_{32}, and phases $\psi_{1,p}$ in the presence of the Doppler effect.

Figure 9 shows the plots of the real and imaginary parts of the Doppler-affected eigenvalues of λ_i, where $i = 1, 2, 3$, versus the mod of Rabi frequency $|\sigma_2|/\gamma$ and probe field detuning Δ_p/γ, Figure 3 shows the same plot without any shifts. The imaginary parts of three eigenvalues of non-Hermitian Hamiltonian coincide at the resonance surface $|\sigma_2| = 2.4\gamma$, which is a second-order exceptional surface of non-Hermitian Hamiltonian in a three-level atomic medium, and the exceptional surface values are 1 and $|\sigma_2| = 2.4\gamma$. The two eigenvalues λ_1 and λ_3 show degeneracy in the range of $1\gamma \leq |\sigma_2| \leq 2.4\gamma$ and $-10\gamma \leq \Delta_p \leq 10\gamma$. The imaginary part of three eigenvalues coincides at exceptional surface values of 0 and $|\sigma_2| = 1\gamma$ and shows degeneracy in the range of $0\gamma \leq |\sigma_2| \leq 1\gamma$ and $-10\gamma \leq \Delta_p \leq 10\gamma$, as illustrated

in Figure 9. The real part of λ_i shows one third-order exceptional surface. The three eigenvalues λ_i coincide at resonance surface $|\sigma_2| = 17\gamma$, and exceptional surface values are 0 and $|\sigma_2| = 17\gamma$, showing degeneracy in the range of $17\gamma \leq |\sigma_2| \leq 20\gamma$ and $-10\gamma \leq \Delta_p \leq 10\gamma$, as illustrated in Figure 9.

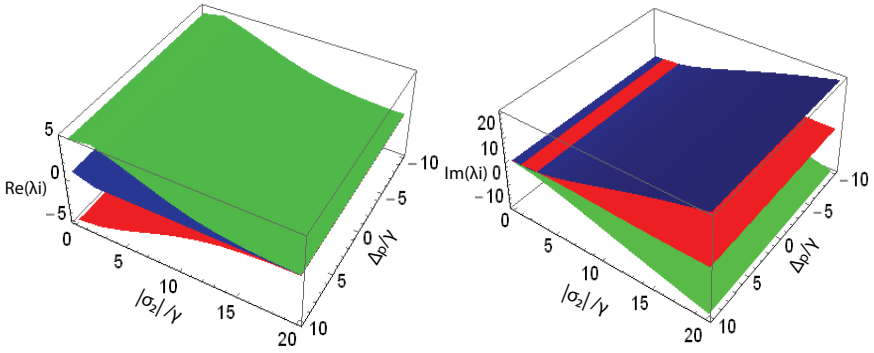

Figure 9. The real and imaginary parts of eigenvalues versus Rabi frequency σ_2 and detuning Δ_p. Other parameter values are $\gamma_{21} = 0.89\gamma$, $\gamma_{32} = 0.98\gamma$, $\Delta_1 = -0.5\gamma$, $\Delta_2 = 0.5\gamma$, $|\sigma_p| = 2\gamma$, $|\sigma_1| = 0.5\gamma$, $\psi_p = 2\pi$, $\psi_1 = \pi$, $\psi_2 = \pi/2$.

Figure 10 shows the plots for real and imaginary parts of Doppler-affected eigenvalues of λ_i, where $i = 1, 2, 3$, versus the mod of Rabi frequency $|\sigma_1|/\gamma$ and phase angle ψ_p. Figure 4 shows the same plot without any shift. The imaginary parts of three eigenvalues of a non-Hermitian Hamiltonian show two second-order exceptional surfaces. The two eigenvalues λ_1 and λ_3 coincide at the resonance surface $|\sigma_1| = 3.8\gamma$, and exceptional surface values are 1 and $|\sigma_1| = 3.8\gamma$, showing degeneracy in the range of $0 \leq \psi_p \leq 2\pi$. The two eigenvalues λ_1 and λ_2 coincide at resonance surface $|\sigma_1| = 5\gamma$, and exceptional surface values are 0 and $|\sigma_1| = 5\gamma$ showing degeneracy in the range of $4\gamma \leq |\sigma_1| \leq 5\gamma$ and $0 \leq \psi_p \leq 2\pi$, as illustrated in Figure 10. The real part of λ_i shows two second-order exceptional surfaces. The two eigenvalues λ_2 and λ_3 coincide at resonance surface $|\sigma_1| = 4\gamma$, and exceptional surface values are 0 and $|\sigma_1| = 4\gamma$, showing degeneracy in the range of $0 \leq \psi_p \leq 2\pi$. The two eigenvalues λ_1 and λ_3 coincide at resonance surface $|\sigma_1| = 2.2\gamma$, and exceptional surface values are -20 and $|\sigma_1| = 2.2\gamma$, showing degeneracy in the range of $0\gamma \leq |\sigma_1| \leq 2.2\gamma$ and $0 \leq \psi_p \leq 2\pi$, as illustrated in Figure 10.

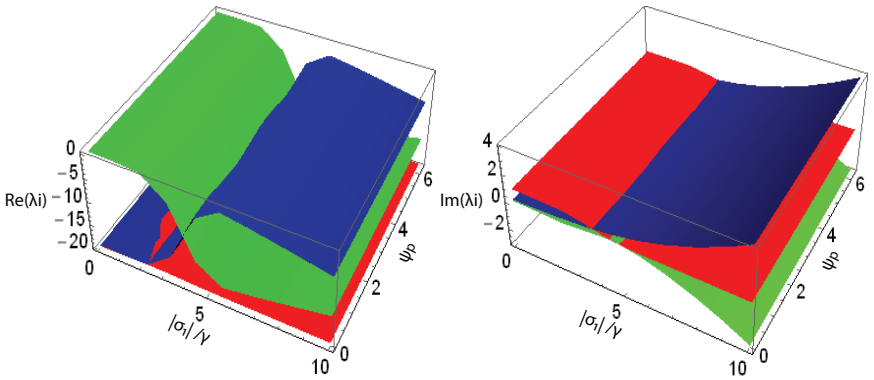

Figure 10. The real and imaginary parts of eigenvalues versus Rabi frequency σ_1 and phase ψ_p. Other parameter values are $\gamma_{21} = 0.09\gamma$, $\gamma_{32} = 0.08\gamma$, $\Delta_1 = -20\gamma$, $\Delta_p = 20\gamma$,$\Delta_2 = -20\gamma$, $|\sigma_2| = 0.1\gamma$, $|\sigma_p| = 0.1\gamma$, $\psi_1 = \pi/2$, $\psi_2 = 0.4\pi$.

Figure 11 shows the plots for the real and imaginary parts of Doppler-effected eigenvalues of λ_i, where $i = 1, 2, 3$, versus the mod of Rabi frequency $|\sigma_p|/\gamma$ and decay rate γ_{21}. Figure 5 shows the same plot without any shift. The imaginary part shows one third-order and one second-order exceptional surface. The imaginary part of three eigenvalues of a non-Hermitian Hamiltonian coincides at the resonance surface $|\sigma_p| = 16\gamma$. This is a third-order exceptional surface of a non-Hermitian Hamiltonian in a three-level atomic medium, and the exceptional surface values are 0 and $|\sigma_p| = 16\gamma$. The three eigenvalues show degeneracy in the range of $0\gamma \leq |\sigma_p| \leq 16\gamma$ and $0 \leq \gamma_{21} \leq 2$. The two eigenvalues λ_1 and λ_3 coincide at resonance surface $|\sigma_p| = 21\gamma$, and exceptional surface values are 4 and $|\sigma_p| = 21\gamma$, showing degeneracy in the range of $16\gamma \leq |\sigma_p| \leq 21\gamma$, as illustrated in Figure 11. The real part of λ_i shows six second-order exceptional surfaces. The two eigenvalues λ_2 and λ_3 coincide at four resonance surfaces: $|\sigma_p| = 5\gamma$, $|\sigma_p| = 11\gamma$, $|\sigma_p| = 16\gamma$, and $|\sigma_p| = 26\gamma$, and exceptional surface values are 6 and $|\sigma_p| = 5\gamma$ and 3 and $|\sigma_p| = 11\gamma$ and 2 and $|\sigma_p| = 16\gamma$, and others are -5 and $|\sigma_p| = 26\gamma$, which show degeneracy in the range of $26\gamma \leq |\sigma_p| \leq 30\gamma$ and $0 \leq \gamma_{21} \leq 2$. The two eigenvalues λ_1 and λ_3 coincides at resonance surface $|\sigma_p| = 21\gamma$, and exceptional surface values are -2 and $|\sigma_p| = 21\gamma$. The other two eigenvalues λ_1 and λ_2 coincide at resonance surface $|\sigma_p| = 23\gamma$ and exceptional surface values are -4 and $|\sigma_p| = 23\gamma$, as illustrated in Figure 11.

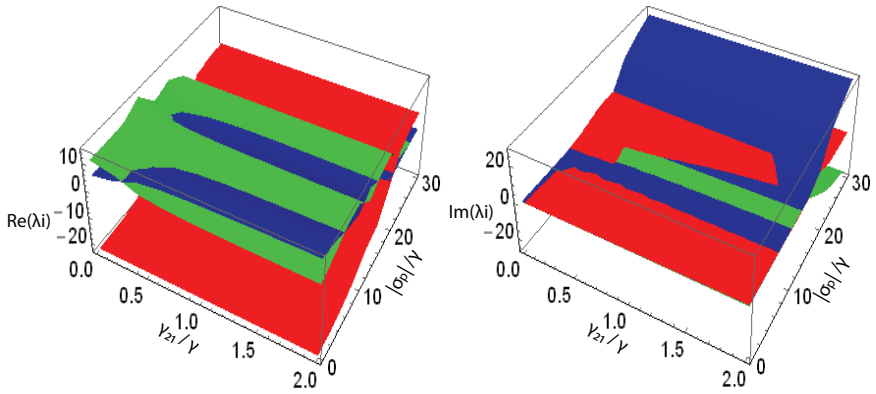

Figure 11. The real and imaginary parts of eigenvalues versus Rabi frequency σ_p and decay rate γ_{21}. Other parameter values are $\gamma_{21} = 0.89\gamma$, $\gamma_{32} = 0.98\gamma$, $\Delta_1 = -0.5\gamma$, $\Delta_2 = 0.5\gamma$, $|\sigma_p| = 2\gamma$, $|\sigma_1| = 0.5\gamma$, $\psi_p = 2\pi$, $\psi_1 = \pi$, $\psi_2 = \pi/2$.

Figure 12 shows the plots for the Doppler-affected real part of eigenstate $S_i(t)$, where $i = 1, 2, 3$, against Rabi frequency of probe and control fields $\sigma_{p,2}/\gamma$ and normalized time t/τ, where as the same plot without any shift is shwon in Figure 7. Figure 12(a) is plotted for the real part of the eigenstate against Rabi frequency σ_p/γ and time t/τ. The eigenstate is the function of Rabi frequency of probe field σ_p and time coordinate t/τ. The three eigenstates of $S_i(t)$ coincide at $\sigma_p = 3\gamma$, where the exceptional surface values are 0 and $\sigma_p = 3\gamma$. The eigenstate one and eigenstate three coincide at resonance point $\sigma_p = 0\gamma$, where the exceptional surface values are 0 and $\sigma_p = 0\gamma$, while the other two eigenstates, one and two coincide at resonance point $\sigma_p = 0.5\gamma$, where the exceptional surface values are -5 and $\sigma_p = 0.5\gamma$. The exceptional surfaces are controlled at Rabi frequencies $\sigma_1 = 15\gamma$, $\sigma_2 = 0.2\gamma$, detuning $\Delta_{2,3} = 0\gamma$, $\Delta_1 = 8\gamma$, decay rates, $\gamma_{21,32} = 0.1\gamma$ and phases, $\psi_{1,2,p} = 0$. Figure 12(b) shows the real part of the eigenstate against control field detuning σ_2/γ and time t/τ. The eigenstate is the function of Rabi frequency of probe field σ_2/γ and time coordinate t/τ. The exceptional surfaces are controlled at Rabi frequencies $\sigma_1 = 5\gamma$, $\sigma_p = 0.1\gamma$, detuning $\Delta_{1,2} = 0\gamma$, $\Delta_p = 0.002\gamma$, decay rates, $\gamma_{21,32} = 0.001\gamma$ and phases, $\psi_{1,2,p} = 0$. The three eigenstates of $S_i(t)$ coincide at multiple points and

show multiple exceptional surfaces and maximum degeneracy.

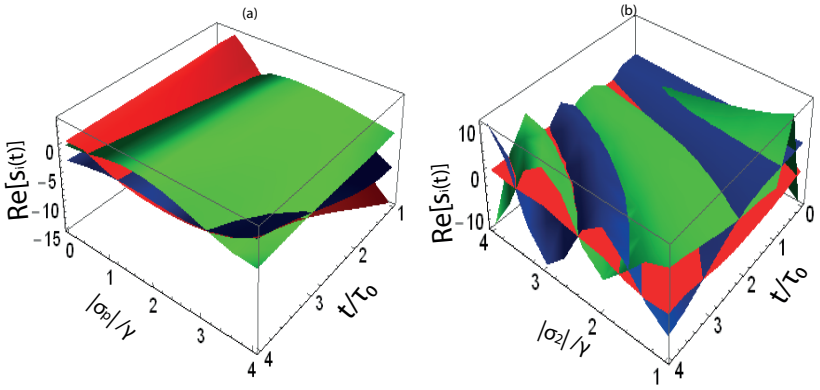

Figure 12. The real part of eigenstate versus Rabi frequency $\sigma_{p,2}$ and time t/τ. Other parameter values are (a) $\sigma_1 = 15\gamma$, $\sigma_2 = 0.2\gamma$, $\Delta_1 = 8\gamma$, $\Delta_{2,p} = 0\gamma$, $\gamma_{21,32} = 0.1\gamma$, $\psi_{1,2,p} = 0$, (b) $\sigma_p = 0.1\gamma$, $\sigma_1 = 5\gamma$, $\Delta_1 = 0.002\gamma$, $\Delta_{1,2} = 0\gamma$, $\gamma_{21,32} = 0.001\gamma$, $\psi_{1,2,p} = 0$.

Figure 13 shows the Doppler-affected real part of the eigenstate $S_i(t)$, where $i = 1, 2, 3$, against Rabi frequency σ_1/γ, detuning Δ_2/γ and normalized time t/τ, where as the same plot without any shifts is shown in Figure 8. Figure 13(a) shows the real part of the eigenstate against Rabi frequency σ_1/γ and time t/τ. The eigenstate is the function of Rabi frequency σ_1 and time coordinate t/τ. The three eigenstates show degeneracy, which decreases along Rabi frequency σ_1, and time coordinate. The three eigenstates of $S_i(t)$ coincide at $\sigma_1 = 1\gamma$ where the exceptional surface values are 0 and $\sigma_1 = 1\gamma$. The three eigenstates of three-level non-Hermitian Hamiltonian show degeneracy in the region enclosed by the range $0\gamma \leq |\sigma_1| \leq 3\gamma$ and $0\tau \leq |t| \leq 4\tau$. The exceptional surfaces are controlled at Rabi frequencies $\sigma_p = 0.1\gamma$, $\sigma_2 = 0.2\gamma$, detuning $\Delta_{1,2,3} = 0\gamma$, decay rates, $\gamma_{21} = 0.4\gamma$, $\gamma_{32} = 0.3\gamma$ and phases, $\psi_{1,2,p} = 0$. Figure 13(b) shows the real part of the eigenstate against the control field detuning Δ_2/γ and time t/τ. The eigenstate is the function of detuning Δ_2 and time coordinate t/τ. The exceptional surfaces are controlled at Rabi frequencies $\sigma_{1,2,p} = 0.01\gamma$, detuning $\Delta_1 = 0.1\gamma$, $\Delta_p = 2\gamma$, decay rates, $\gamma_{21} = 0.8\gamma$, $\gamma_{32} = 0.9\gamma$ and phases, $\psi_{1,2,p} = 0$. The three eigenstates of $S_i(t)$ coincide at $\Delta_2 = 1\gamma$, where the exceptional surface values are 0 and $\Delta_2 = 1\gamma$. The three eigenstates of three-level non-Hermitian Hamiltonian show degeneracy in the range of $1\gamma \leq |\Delta_2| \leq 4\gamma$, which decrease along time coordinate t/τ.

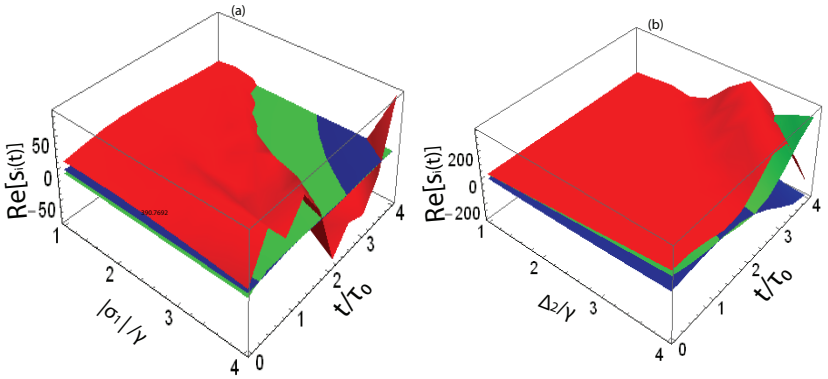

Figure 13. The real part of eigenstate versus Rabi frequency σ_1, detuning Δ_2/γ and time t/τ. Other parameter values are (a). $\sigma_1 = 15\gamma$, $\sigma_2 = 0.2\gamma$, $\Delta_1 = 8\gamma$, $\Delta_{2,p} = 0\gamma$, $\gamma_{21,32} = 0.1\gamma$, $\psi_{1,2,p} = 0$, (b). $\sigma_p = 0.1\gamma$, $\sigma_1 = 5\gamma$, $\Delta_1 = 0.002\gamma$, $\Delta_{1,2} = 0\gamma$, $\gamma_{21,32} = 0.001\gamma$, $\psi_{1,2,p} = 0$.

3.3. *Smaller and larger Doppler width V_D*

For comparison, consider the plot for the real and imaginary parts of eigenvalues of λ_i, where i=1, 2, 3, versus the mod of Rabi frequency $|\sigma_p|/\gamma$ and decay rate γ_{21}, at a smaller value of Doppler width, at a larger value of Doppler width, and in the absence of the Doppler-affect. The latter is illustrated in Figure 5, whereas the other two cases are discussed here.

Figure 14 shows the imaginary parts of eigenvalues of λ_i, where i = 1, 2, 3, versus the mod of Rabi frequency $|\sigma_p|/\gamma$ and decay rate γ_{21} at larger and smaller Doppler width V_D. The imaginary parts of three eigenvalues of a non-Hermitian Hamiltonian are studied at a smaller Doppler width V_D=0.1γ. The imaginary part shows one third-order and two second-order exceptional surfaces. The three eigenvalues coincide at the resonance surface $|\sigma_p| = 13\gamma$. This is a third-order exceptional surface of a non-Hermitian Hamiltonian in a three-level atomic medium, and the exceptional surface values are 0 and $|\sigma_p| = 13\gamma$. The three eigenvalues show degeneracy in the range of $0\gamma \leq |\sigma_p| \leq 13\gamma$ and $0 \leq \gamma_{21} \leq 2$. The two eigenvalues λ_2 and λ_3 coincide at resonance surface $|\sigma_p| = 18\gamma$, and exceptional surface values are 4 and $|\sigma_p| = 18\gamma$. The other two eigenvalues λ_1 and λ_2 coincide at resonance surface $|\sigma_p| = 20\gamma$, and exceptional surface values are -3 and $|\sigma_p| = 20\gamma$, shown in Figure 14. Again, the imaginary parts of three eigenvalues of a non-Hermitian Hamiltonian are studied at a larger Doppler width $V_D = 11\gamma$. The imaginary part shows one third-order exceptional surface. The three eigenvalues coincide at the resonance surface $|\sigma_p| = 17\gamma$. This is a third-order exceptional surface of a non-Hermitian Hamiltonian in a three-level atomic medium, and the exceptional surface values are 0 and $|\sigma_p| = 17\gamma$. The three eigenvalues show degeneracy in the range of $0\gamma \leq |\sigma_p| \leq 17\gamma$ and $0 \leq \gamma_{21} \leq 2$, as shown in Figure 14. Here, the overall results show that the degeneracy increases in the imaginary part of eigenvalues with an increase in Doppler width V_D.

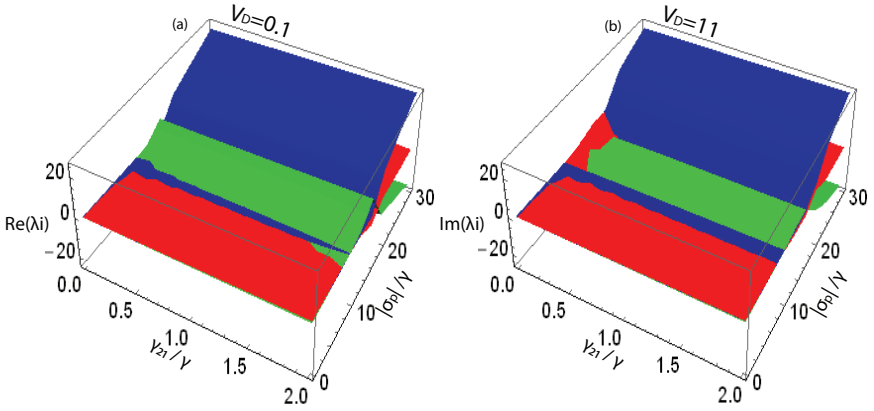

Figure 14. The imaginary part of eigenvalues versus Rabi frequency σ_p and decay rate γ_{21}. Other parameter values are $\gamma_{32} = 0.1\gamma$, $\Delta_1 = -2.5\gamma$, $\Delta_2 = -4.5\gamma$, $\Delta_p = -1.5\gamma$, $|\sigma_1| = 12\gamma$, $|\sigma_2| = 15\gamma$, $\psi_1 = \pi/2$, $\psi_1 = \pi$, $\psi_2 = \pi$.

Figure 15 shows the real parts of eigenvalues of λ_i, where $i = 1, 2, 3$ versus the mod of Rabi frequency $|\sigma_p|/\gamma$ and decay rate γ_{21} at larger and smaller Doppler width V_D. The real parts of three eigenvalues of a non-Hermitian Hamiltonian are studied at a smaller Doppler width $V_D = 0.1\gamma$. The real part of λ_i shows five second-order exceptional surfaces. The two eigenvalues λ_2 and λ_3 coincide at three resonance surfaces, $|\sigma_p| = 4\gamma$, $|\sigma_p| = 10\gamma$, and $|\sigma_p| = 21\gamma$, and exceptional surface values are 6 and $|\sigma_p| = 4\gamma$ and 3 and $|\sigma_p| = 10\gamma$, and others are -5 and $|\sigma_p| = 21\gamma$, which show degeneracy

in the range of $21\gamma \leq |\sigma_p| \leq 30\gamma$ and $0 \leq \gamma_{21} \leq 2$. The two eigenvalues λ_1 and λ_3 coincide at resonance surface $|\sigma_p| = 19\gamma$, and exceptional surface values are 2 and $|\sigma_p| = 19\gamma$. The other two eigenvalues λ_1 and λ_2 coincide at the resonance surface $|\sigma_p| = 17\gamma$, and exceptional surface values are -5 and $|\sigma_p| = 17\gamma$, as shown in Figure 15. Again, the real parts of three eigenvalues of a non-Hermitian Hamiltonian are studied at a larger Doppler width $V_D = 11\gamma$. The real part of λ_i shows six second-order exceptional surfaces. The two eigenvalues λ_2 and λ_3 coincide at four resonance surfaces $|\sigma_p| = 5\gamma$, $|\sigma_p| = 11\gamma$, $|\sigma_p| = 16\gamma$, and $|\sigma_p| = 23\gamma$, and exceptional surface values are 6 and $|\sigma_p| = 5\gamma$, 3 and $|\sigma_p| = 11\gamma$, and 2 and $|\sigma_p| = 16\gamma$, and others are -5 and $|\sigma_p| = 24\gamma$, which show degeneracy in the range of $24\gamma \leq |\sigma_p| \leq 30\gamma$ and $0 \leq \gamma_{21} \leq 2$. The two eigenvalues λ_1 and λ_3 coincide at resonance surface $|\sigma_p| = 20\gamma$, and exceptional surface values are -2 and $|\sigma_p| = 20\gamma$. The other two eigenvalues λ_1 and λ_2 coincide at resonance surface $|\sigma_p| = 23\gamma$, and exceptional surface values are -1 and $|\sigma_p| = 23\gamma$, as shown in Figure 15. Here, the overall results show that the degeneracy decreases in the real parts of eigenvalues with an increase in Doppler width V_D.

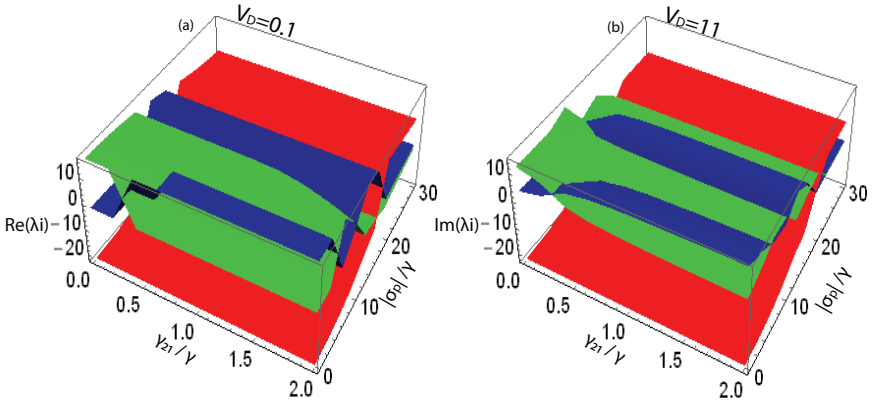

Figure 15. The real part of eigenvalues versus Rabi frequency σ_p and decay rate γ_{21}. Other parameter values are $\gamma_{21} = 0.9\gamma$, $\gamma_{32} = 0.08\gamma$, $\Delta_1 = -20\gamma$, $\Delta_2 = -20\gamma$, $\Delta_p = 18\gamma$, $|\sigma_p| = 0.1\gamma$, $|\sigma_2| = 0.1\gamma$, $\psi_1 = \pi/2$, $\psi_2 = 0.4\pi$, $V_D = 11\gamma$.

3.4. Plots against Doppler width V_D

Figure 16 displays the plots for the real and imaginary parts of eigenvalues of λ_i, where i = 1, 2, 3, versus Doppler width V_D. The imaginary parts show three second-order exceptional points. The two eigenvalues λ_1 and λ_3 coincide at resonance point $V_D = 0\gamma$, and the exceptional point values are 0.4 and $V_D = 0\gamma$. The other two eigenvalues λ_1 and λ_2 coincide at resonance point $V_D = 7\gamma$, which show degeneracy in the range of $7\gamma \leq V_D \leq 40\gamma$, and exceptional point values are 0.1 and $V_D = 7\gamma$. The other two eigenvalues λ_2 and λ_3 coincide at resonance point $V_D = 0\gamma$, and exceptional point values are 0 and $V_D = 0\gamma$. The imaginary part of three eigenvalues shows that degeneracy increases with increasing Doppler width, as illustrated in Figure 16. The real parts of three eigenvalues of a non-Hermitian Hamiltonian coincide at the resonance point $V_D = 0\gamma$; this is a third-order exceptional point of a non-Hermitian Hamiltonian in a three-level atomic medium, and the exceptional point values are 0 and $V_D = 0\gamma$. The three eigenvalues show degeneracy in the range of $0\gamma \leq V_D \leq 3\gamma$. The real part of three eigenvalues shows that degeneracy decreases with increasing Doppler width, as illustrated in Figure 16.

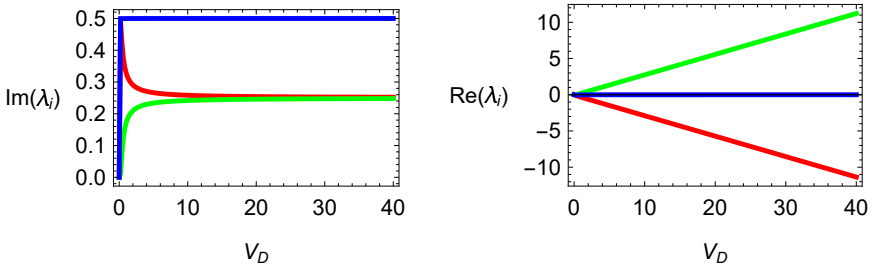

Figure 16. The real and imaginary parts of eigenvalues versus Doppler width V_d. Other parameter values are $\gamma_{21} = 0.5\gamma$, $\gamma_{32} = 0.5\gamma$, $\Delta_1 = -0.15\gamma$, $\Delta_2 = -0.005\gamma$, $\Delta_p = -0.15\gamma$ $|\sigma_1| = 0.015\gamma$, $|\sigma_2| = 0.015\gamma$, $|\sigma_p| = 0.015\gamma$, $\psi_p = \pi$, $\psi_1 = \pi$, $\psi_2 = \pi$.

Figure 17 shows the plots for the real and imaginary parts of eigenvalues of λ_i, where i = 1, 2, 3, versus Doppler width V_D. The imaginary parts show one second-order and one third-order exceptional point. The imaginary parts of three eigenvalues of a non-Hermitian Hamiltonian coincide at the resonance point $V_D = 0\gamma$; this is a third-order exceptional point of a non-Hermitian Hamiltonian in a three-level atomic medium, and the exceptional point values are 0 and $V_D = 0\gamma$. The two eigenvalues λ_1 and λ_3 coincide at resonance point $V_D = 18\gamma$, which show degeneracy in the range of $18\gamma \leq V_D \leq 40\gamma$, and exceptional point values are 1.7 and $V_D = 18\gamma$. The imaginary part of three eigenvalues shows that degeneracy increases with increasing Doppler width, as illustrated in Figure 17. The real parts show two second-order exceptional points. The two eigenvalues λ_2 and λ_3 coincide at resonance point $V_D = 0\gamma$, and exceptional point values are 0 and $V_D = 0\gamma$. The other two eigenvalues λ_1 and λ_3 coincide at resonance point $V_D = 6\gamma$, which show degeneracy in the range of $0\gamma \leq V_D \leq 6\gamma$, and exceptional point values are -3 and $V_D = 6\gamma$. The real part of three eigenvalues shows that degeneracy decreases with increasing Doppler width, as illustrated in Figure 17.

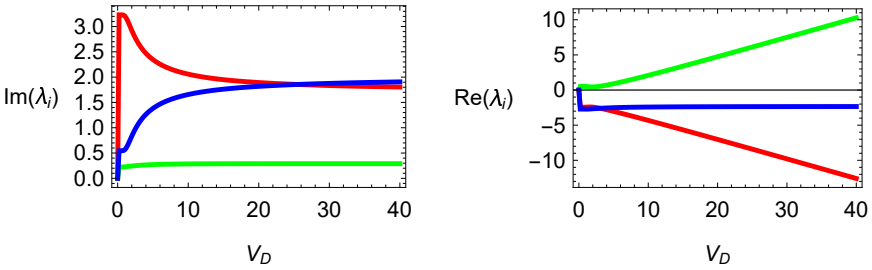

Figure 17. The real and imaginary parts of eigenvalues versus Doppler width V_d. Other parameter values are $\gamma_{21} = 2\gamma$, $\gamma_{32} = 2\gamma$, $\Delta_1 = -2.15\gamma$, $\Delta_2 = -2.5\gamma$, $\Delta_p = -0.0015\gamma$ $|\sigma_1| = 1.0015\gamma$, $|\sigma_2| = 0.00015\gamma$, $|\sigma_p| = 1.015\gamma$, $\psi_p = \pi/2$, $\psi_1 = 2\pi$, $\psi_2 = \pi/2$.

Figure 18 shows the plots for the real and imaginary parts of eigenvalues of λ_i, where i = 1, 2, 3, versus Doppler width V_D. The imaginary parts of three eigenvalues of a non-Hermitian Hamiltonian coincide at the resonance surface $V_D = 0\gamma$; this is a third-order exceptional point of a non-Hermitian Hamiltonian in a three-level atomic medium, and the exceptional point values are 0 and $V_D = 0\gamma$. The imaginary part of three eigenvalues shows that degeneracy decreases with increasing Doppler width, as illustrated in Figure 18. The real parts of three eigenvalues of a non-Hermitian Hamiltonian coincide at the resonance point $V_D = 15\gamma$; this is a third-order exceptional point of a non-Hermitian Hamiltonian in a three-level atomic medium, and the exceptional point values are 0 and $V_D = 15\gamma$. The three

eigenvalues show degeneracy in the range of $0\gamma \leq V_D \leq 15\gamma$. The real part of three eigenvalues shows that degeneracy decreases with increasing Doppler width, as illustrated in Figure 18.

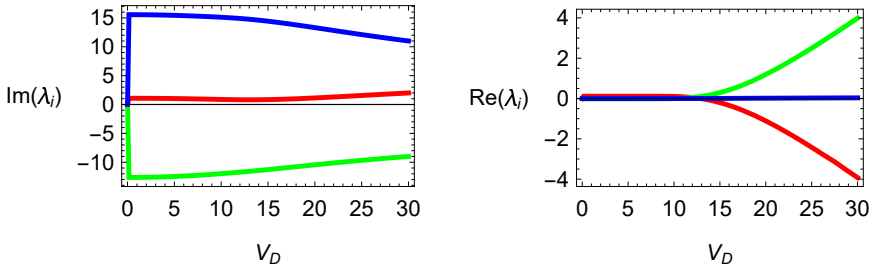

Figure 18. The real and imaginary parts of eigenvalues versus Doppler width V_d. Other parameter values are $\gamma_{21} = 2\gamma$, $\gamma_{32} = 2\gamma$, $\Delta_1 = -0.1\gamma$, $\Delta_2 = 0.2\gamma$, $\Delta_p = -8.2\gamma$ $|\sigma_1| = 10.5\gamma$, $|\sigma_2| = 9.1\gamma$, $|\sigma_p| = 2.1\gamma$, $\psi_p = \pi/2$, $\psi_1 = 2\pi/4$, $\psi_2 = 2\pi/4$.

3.5. In the Presence of the Zeeman shift

In this section, plots are displayed for the real and imaginary parts of eigenvalues versus Rabi frequency $\sigma_{1,2,p}$, detuning $\Delta_{1,p}$, decay rate γ_{32}, and phases $\psi_{1,p}$ in the presence of the Zeeman effect. The Zeeman width is taken as $W_z = 20\gamma$.

Figure 19 shows the plots for the real and imaginary parts of eigenvalues of λ_i, where $i = 1, 2, 3$, versus Rabi frequency $|\sigma_2|/\gamma$ and probe field detuning Δ_p/γ, whereas the same plot without any shift is shown in Figure 3. The imaginary parts of three eigenvalues of a non-Hermitian Hamiltonian show one third-order and one second-order exceptional surface. The two eigenvalues λ_1 and λ_2 coincide at resonance surface $|\sigma_2| = 1\gamma$, and exceptional surface values are 0 and $|\sigma_2| = 1\gamma$, showing degeneracy in the range of $0\gamma \leq |\sigma_2| \leq 1\gamma$ and $-10\gamma \leq \Delta_p \leq 10\gamma$. The imaginary parts of three eigenvalues coincide at the resonance surface $|\sigma_2| = 0\gamma$; this is a third-order exceptional surface of a non-Hermitian Hamiltonian in a three-level atomic medium, and the exceptional surface values are 0 and $|\sigma_2|$=0γ. The three eigenvalues show degeneracy in the range of $-10\gamma \leq \Delta_p \leq 10\gamma$, as illustrated in Figure 19. The real part of λ_i shows one third-order and three second-order exceptional surfaces. The three eigenvalues λ_i coincide at resonance surface $|\sigma_2| = 7.5\gamma$, and exceptional surface values are 0 and $|\sigma_2| = 7.5\gamma$, showing degeneracy in the range of $7.5\gamma \leq |\sigma_2| \leq 20\gamma$ and $-10\gamma \leq \Delta_p \leq 10\gamma$. The two eigenvalues λ_2 and λ_3 coincide at resonance surface $|\sigma_2| = 6\gamma$, and exceptional surface values are 0 and $|\sigma_2| = 6\gamma$, showing degeneracy in the range of $6\gamma \leq |\sigma_2| \leq 7.5\gamma$ and $-10\gamma \leq \Delta_p \leq 10\gamma$. The two eigenvalues λ_1 and λ_3 coincide at resonant point $|\sigma_2| = 1.5\gamma$, and exceptional surface values are 0.001 and $|\sigma_2| = 1.5\gamma$ and show degeneracy in the range of $-10\gamma \leq \Delta_p \leq 10\gamma$. The two eigenvalues λ_1 and λ_2 coincide at resonant point $|\sigma_2| = 0.5\gamma$, and exceptional surface values are -0.002 and $|\sigma_2| = 0.5\gamma$, showing degeneracy in the range of $-10\gamma \leq \Delta_p \leq 10\gamma$, as illustrated in Figure 19.

Figure 20 shows he plots for the real and imaginary parts of eigenvalues of λ_i, where $i = 1, 2, 3$, versus Rabi frequency $|\sigma_1|/\gamma$ and phase angle ψ_p, whereas the same plot without any shift is demonstrated in Figure 4. The imaginary parts of three eigenvalues of a non-Hermitian Hamiltonian coincide at the resonance surface $|\sigma_1| = 9\gamma$. This is a third-order exceptional surface of a non-Hermitian Hamiltonian in a three-leve atomic medium, and the exceptional surface values are 0 and $|\sigma_1| = 9\gamma$. The three eigenvalues show degeneracy in the range of $0\gamma \leq |\sigma_1| \leq 9\gamma$ and $0 \leq \psi_p \leq 2\pi$, as illustrated in Figure 20. The real part of λ_i shows four second-order exceptional surfaces. The two eigenvalues

λ_2 and λ_3 coincide at resonance surface $|\sigma_1| = 13\gamma$, and exceptional surface values are -0.10 and $|\sigma_1| = 13\gamma$, showing degeneracy in the range of $13\gamma \leq |\sigma_1| \leq 20\gamma$ and $0 \leq \psi_p \leq 2\pi$. The two eigenvalues λ_2 and λ_3 coincide at resonance surface $|\sigma_1| = 9.5\gamma$, and exceptional surface values are -0.025 and $|\sigma_1| = 9.5\gamma$, showing degeneracy in the range of $0 \leq \psi_p \leq 2\pi$. The two eigenvalues λ_2 and λ_3 coincide at resonance surface $|\sigma_1| = 3.9\gamma$, and exceptional surface values are -0.025 and $|\sigma_1| = 3.9\gamma$, showing degeneracy in the range of $0 \leq \psi_p \leq 2\pi$. The two eigenvalues λ_1 and λ_3 coincide at resonance surface $|\sigma_1| = 2.9\gamma$, and exceptional surface values are -0.045 and $|\sigma_1| = 2.9\gamma$, showing degeneracy in the range of $0\gamma \leq |\sigma_1| \leq 2.9\gamma$ and $0 \leq \psi_p \leq 2\pi$, as illustrated in Figure 20.

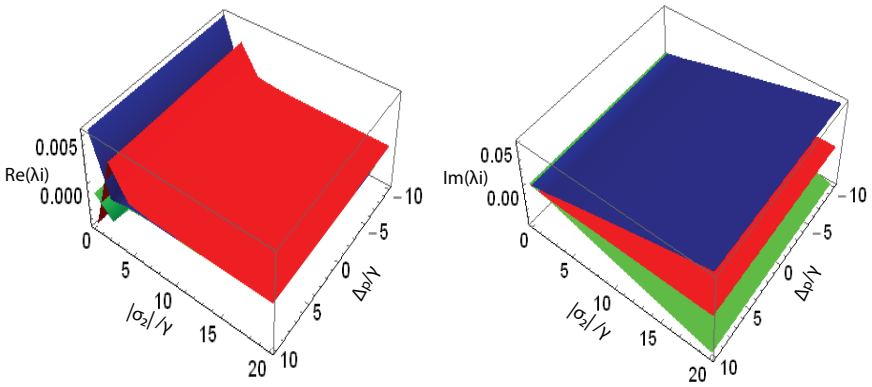

Figure 19. The real and imaginary parts of eigenvalues versus Rabi frequency σ_2 and detuning Δ_p. Other parameter values are $\gamma_{21} = 0.89\gamma$, $\gamma_{32} = 0.98\gamma$, $\Delta_1 = -0.5\gamma$, $\Delta_2 = 0.5\gamma$, $|\sigma_p| = 2\gamma$, $|\sigma_1| = 0.5\gamma$, $\psi_p = 2\pi$, $\psi_1 = \pi$, $\psi_2 = \pi/2$.

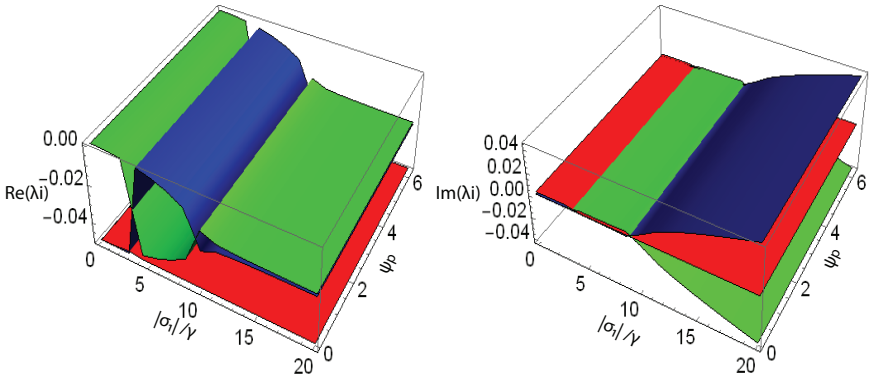

Figure 20. The real and imaginary parts of eigenvalues versus Rabi frequency σ_1 and phase ψ_p. Other parameter values are $\gamma_{21} = 0.9\gamma$, $\gamma_{32} = 0.08\gamma$, $\Delta_1 = -20\gamma$, $\Delta_2 = -20\gamma$ $\Delta_p = 18\gamma$, $|\sigma_p| = 0.1\gamma$, $|\sigma_2| = 0.1\gamma$, $\psi_1 = 0.5\pi$, $\psi_2 = 0.4\pi$.

Figure 21 shows the plots for the real and imaginary parts of eigenvalues of λ_i, where $i = 1, 2, 3$, versus Rabi frequency $|\sigma_p|/\gamma$ and decay rate γ_{32}/γ. The imaginary parts of three eigenvalues of non-Hermitian Hamiltonian coincide at the resonance surface $|\sigma_p| = 10\gamma$; this is a third-order exceptional surface of non-Hermitian Hamiltonian in a three-level atomic medium, and the exceptional surface values are 0 and $|\sigma_p| = 10\gamma$. The three eigenvalues show degeneracy in the range of $0\gamma \leq |\sigma_p| \leq 10\gamma$ and $0\gamma \leq \gamma_{32} \leq 1\gamma$, as illustrated in Figure 21. The real part of λ_i shows two second-order exceptional

surfaces. The two eigenvalues λ_2 and λ_3 coincide at resonance surface $|\sigma_p| = 10\gamma$, and exceptional surface values are 10 and $|\sigma_p| = 10\gamma$, showing degeneracy in the range of $10\gamma \leq |\sigma_p| \leq 30\gamma$ and $0\gamma \leq \gamma_{32} \leq 1\gamma$. The two eigenvalues λ_1 and λ_2 coincide at resonance surface $|\sigma_p| = 2\gamma$, and exceptional surface values are 0 and $|\sigma_p| = 2\gamma$, showing degeneracy in the range of $0\gamma \leq |\sigma_p| \leq 2\gamma$ and $0\gamma \leq \gamma_{32} \leq 1\gamma$. In this case, the Zeeman shift does not change the exceptional surface value or degeneracy but changes the shape of eigenvalues, as illustrated in Figure 21.

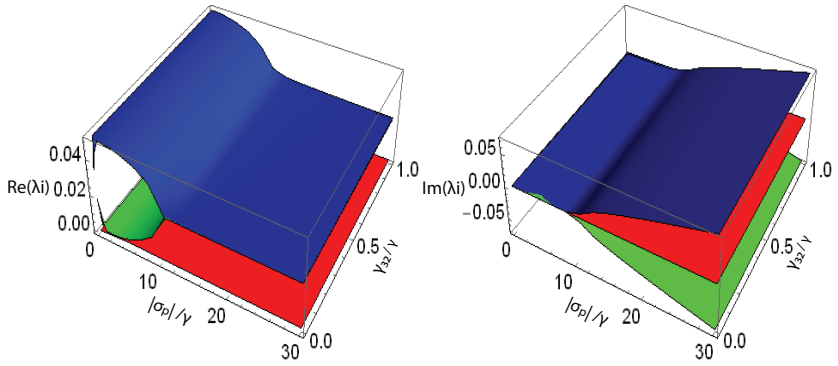

Figure 21. The real and imaginary parts of eigenvalues versus Rabi frequency σ_p and decay rate γ_{32}. Other parameter values are $\gamma_{21} = 0.001\gamma$, $\Delta_1 = 0.0001\gamma$, $\Delta_2 = 20\gamma$, $\Delta_p = 2\gamma$, $|\sigma_1| = 0.02\gamma$, $|\sigma_2| = 3\gamma$, $\psi_1 = \pi/10$,$\psi_2 = 2\pi/2$, $\psi_p = \pi/2$.

Figure 22 shows the plots for the real and imaginary parts of eigenvalues of λ_i, where $i = 1, 2, 3$, versus controlled field detuning Δ_1 and phase angle ψ_1. The imaginary parts of three eigenvalues show two second-order exceptional surfaces. The two eigenvalues λ_2 and λ_3 coincide at the resonance surface $\Delta_1 = 0\gamma$ and exceptional surface values are 0.0025 and $\Delta_1 = 0\gamma$, showing degeneracy in the range of $0 \leq \psi_1 \leq 2\pi$. The other two eigenvalues λ_1 and λ_2 coincide at the resonance surface $\Delta_1 = 0.7\gamma$, and exceptional surface values are 0 and $\Delta_1 = 0.7\gamma$, showing degeneracy in the range of $0 \leq \psi_1 \leq 2\pi$ as illustrated in Figure 22. The real part of λ_i shows two second-order exceptional surfaces. The two eigenvalues λ_2 and λ_3 coincide at resonance surface $\Delta_1 = 1.5\gamma$, and exceptional surface values are 0.02 and $\Delta_1 = 1.5\gamma$, showing degeneracy in the range of $1.5\gamma \leq \Delta_1 \leq 10\gamma$ and $0 \leq \psi_1 \leq 2\pi$. The other two eigenvalues λ_1 and λ_2 coincide at resonance surface $\Delta_1 = -1.5\gamma$, and exceptional surface values are 0 and $\Delta_1 = -1.5\gamma$, showing degeneracy in the range of $-1.5\gamma \leq \Delta_1 \leq -10\gamma$ and $0 \leq \psi_1 \leq 2\pi$, as illustrated in Figure 22.

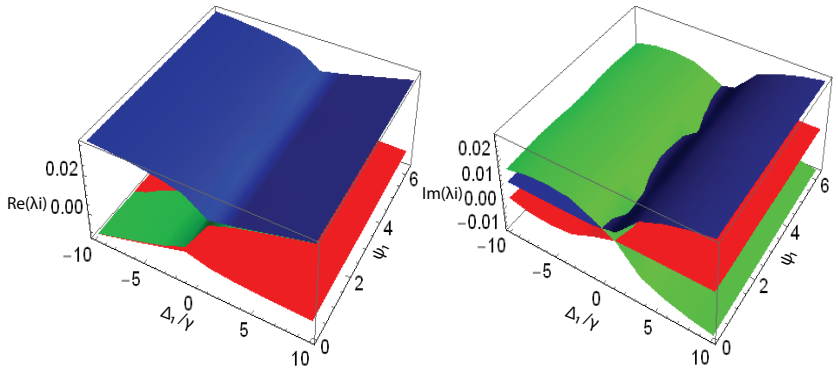

Figure 22. The real and imaginary parts of eigenvalues versus Rabi frequency Δ_1 and phase ψ_1. Other parameter values are $\gamma_{21} = 0.3\gamma$, $\gamma_{32} = 0.6\gamma$, $\Delta_p = 10\gamma$,$\Delta_2 = 15\gamma$, $|\sigma_1| = 1\gamma$, $|\sigma_p| = 6.5\gamma$, $|\sigma_2| = 0.05\gamma$, $\psi_p = \pi/2$, $\psi_2 = \pi/2$.

Figure 23 shows the plots for the Zeeman-affected real part of eigenstate $S_i(t)$, where $i = 1, 2, 3$, against Rabi frequency of probe and control fields $\sigma_{p,2}/\gamma$ and normalized time t/τ, whereas the same plot without any shift is shown in Figure 7. Figure 23(a) plots the real part of eigenstate against Rabi frequency σ_p/γ and time t/τ. The eigenstate is the function of Rabi frequency of probe field σ_p and time coordinate t/τ. The three eigenstates of $S_i(t)$ coincide at two resonance points $\sigma_p = 1.2\gamma$, and $\sigma_p = 2.1\gamma$ where the exceptional surface values are 0 and $\sigma_p = 1.2\gamma$ and the others are 0 and $\sigma_p = 2.1\gamma$. The eigenstate $S_1(t)$ and eigenstate $S_3(t)$ coincide at resonance point $\sigma_p = 3.2\gamma$, where the exceptional surface values are 0 and $\sigma_p = 3.2\gamma$, while eigenstate $S_1(t)$ and eigenstate $S_2(t)$ coincide at resonance point $\sigma_p = 4\gamma$, where the exceptional surface values are 0 and $\sigma_p = 4\gamma$. The exceptional surfaces are controlled at Rabi frequencies $\sigma_1 = 15\gamma$, $\sigma_2 = 0.2\gamma$, detuning $\Delta_{2,3} = 0\gamma$, $\Delta_1 = 8\gamma$, decay rates, $\gamma_{21,32} = 0.1\gamma$ and phases, $\psi_{1,2,p} = 0$. Figure 23(b) shows the real part of eigenstate against Rabi frequency of control field σ_2/γ and time t/τ. The eigenstate is the function of Rabi frequency of control field σ_2/γ and time coordinate t/τ. The eigenstates of $S_i(t)$ coincide at seven resonance points $\sigma_2 = 0.9\gamma$, $\sigma_2 = 1.1\gamma$, $\sigma_2 = 1.9\gamma$, $\sigma_2 = 2.2\gamma$, $\sigma_2 = 3.1\gamma$, $\sigma_2 = 3.3\gamma$, and $\sigma_2 = 3.9\gamma$ and show seven second-order exceptional surfaces. The exceptional surfaces are controlled at Rabi frequencies $\sigma_1 = 5\gamma$, $\sigma_p = 0.1\gamma$, detuning $\Delta_{1,2} = 0\gamma$, $\Delta_p = 0.002\gamma$, decay rates, $\gamma_{21,32} = 0.001\gamma$ and phases, $\psi_{1,2,p} = 0$.

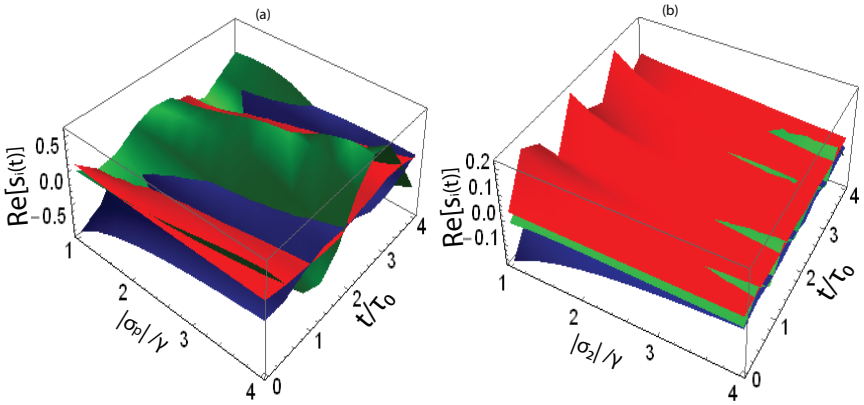

Figure 23. The real part of eigenstate versus Rabi frequency $\sigma_{p,2}$ and time t/τ. Other parameter values are (a) $\sigma_1 = 15\gamma$, $\sigma_2 = 0.2\gamma$, $\Delta_1 = 8\gamma$, $\Delta_{2,p} = 0\gamma$, $\gamma_{21,32} = 0.1\gamma$, $\psi_{1,2,p} = 0$ (b) $\sigma_p = 0.1\gamma$, $\sigma_1 = 5\gamma$, $\Delta_1 = 0.002\gamma$, $\Delta_{1,2} = 0\gamma$, $\gamma_{21,32} = 0.001\gamma$, $\psi_{1,2,p} = 0$.

Figure 24 presents the plots for the Zeeman-affected real part of eigenstate $S_i(t)$, where $i = 1, 2, 3$, against Rabi frequency σ_1/γ, detuning Δ_2/γ, and normalized time t/τ, whereas the same plot without any shifts is shown in Figure 8. Figure 24(a) shows the real part of eigenstate against Rabi frequency σ_1/γ and time t/τ. The eigenstate is the function of Rabi frequency σ_1 and time coordinate t/τ. The two eigenstates of $S_2(t)$ and $S_3(t)$ coincide at $\sigma_1 = 0.2\gamma$, where the exceptional surface values are 0 and $\sigma_1 = 0.2\gamma$. The exceptional surface are controlled at Rabi frequencies $\sigma_p = 0.1\gamma$, $\sigma_2 = 0.2\gamma$, detuning $\Delta_{1,2,3} = 0\gamma$, decay rates, $\gamma_{21} = 0.4\gamma$, $\gamma_{32} = 0.3\gamma$ and phases, $\psi_{1,2,p} = 0$. Figure 24(b) shows the real part of the eigenstate against control field detuning Δ_2/γ and time t/τ. The eigenstate is the function of detuning Δ_2 and time coordinate t/τ. The exceptional surfaces are controlled at Rabi frequencies $\sigma_{1,2,p} = 0.01\gamma$, detuning $\Delta_1 = 0.1\gamma$, $\Delta_p = 2\gamma$, decay rates, $\gamma_{21} = 0.8\gamma$, $\gamma_{32} = 0.9\gamma$ and phases, $\psi_{1,2,p} = 0$. The three eigenstates of $S_i(t)$ coincide at $\Delta_2 = 0.3\gamma$ where the exceptional surface values are 0 and $\Delta_2 = 0.3\gamma$. The three eigenstates of three-level non-Hermitian Hamiltonian show degeneracy in the range of $0.3\gamma \leq |\Delta_2| \leq 1\gamma$, which decrease along the time coordinate t/τ.

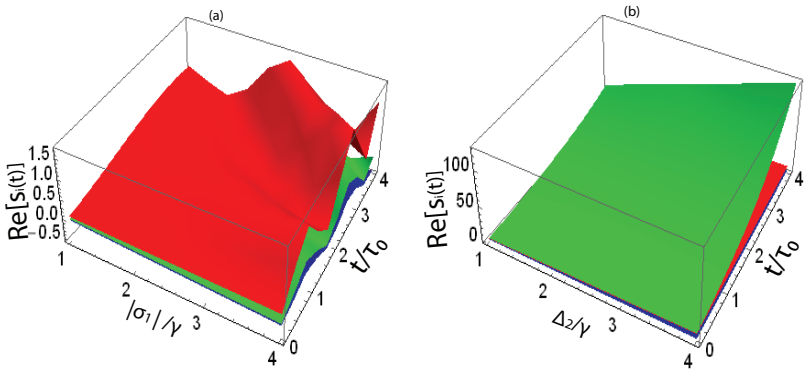

Figure 24. The real part of eigenstate versus Rabi frequency σ_1, detuning Δ_2/γ and time t/τ. Other parameter values are (a). $\sigma_1 = 15\gamma$, $\sigma_2 = 0.2\gamma$, $\Delta_1 = 8\gamma$, $\Delta_{2,p} = 0\gamma$, $\gamma_{21,32} = 0.1\gamma$, $\psi_{1,2,p} = 0$, (b). $\sigma_p = 0.1\gamma$, $\sigma_1 = 5\gamma$, $\Delta_1 = 0.002\gamma$, $\Delta_{1,2} = 0\gamma$, $\gamma_{21,32} = 0.001\gamma$, $\psi_{1,2,p} = 0$.

3.6. Smaller and larger Zeeman width W_z

For comparison, consider the plot for the real and imaginary parts of eigenvalues of λ_i, where $i = 1, 2, 3$, versus the mod of Rabi frequency $|\sigma_1|/\gamma$ and Phase ψ_p, at a smaller value of Zeeman width, at a larger value of Zeeman width, and in absence of Zeeman effect. The latter is shwon in Figure 4, whereas the other two cases are discussed here.

Figure 25 shows the plots for the imaginary parts of eigenvalues of λ_i, where $i = 1, 2, 3$, verses the mod of Rabi frequency $|\sigma_1|/\gamma$ and phase angle ψ_p at larger and smaller Zeeman width W_z. The imaginary parts of three eigenvalues of a non-Hermitian Hamiltonian are studied at a smaller Zeeman width $W_z = 0.1\gamma$. The imaginary parts of three eigenvalues coincide at the resonance surface $|\sigma_1| = 5\gamma$. This is a third-order exceptional surface of a non-Hermitian Hamiltonian in a three-level atomic medium, and the exceptional surface values are 0 and $|\sigma_1| = 5\gamma$. The three eigenvalues show degeneracy in the range of $0\gamma \leq |\sigma_1| \leq 5\gamma$ and $0 \leq \psi_p \leq 2\pi$, as viewed in Figure 25(a). Again, the imaginary parts of three eigenvalues of a non-Hermitian Hamiltonian are studied at a larger Zeeman width, $W_z = 10\gamma$. The imaginary parts of three eigenvalues coincide at the resonance surface $|\sigma_1| = 9\gamma$. This is a third-order exceptional surface of a non-Hermitian Hamiltonian in a three-level atomic medium, and the exceptional surface values are 0 and $|\sigma_1| = 9\gamma$. The three eigenvalues show degeneracy in the range of $0\gamma \leq |\sigma_1| \leq 9\gamma$ and $0 \leq \psi_p \leq 2\pi$, as viewed in Figure 25(b). Here, the overall results show that the degeneracy increases in the imaginary part of eigenvalues with an increase in Zeeman width W_z.

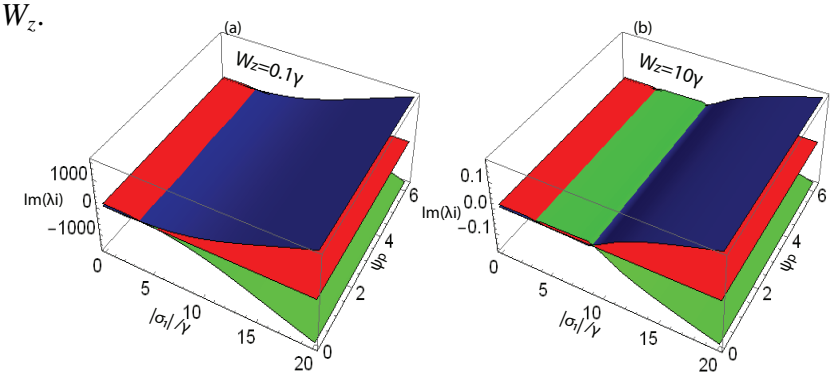

Figure 25. The imaginary part of eigenvalues versus Rabi frequency σ_1 and phase ψ_p. Other parameter values are $\gamma_{21} = 0.9\gamma$, $\gamma_{32} = 0.08\gamma$, $\Delta_1 = -20\gamma$, $\Delta_2 = -20\gamma$,$\Delta_p = 18\gamma$, $|\sigma_p| = 0.1\gamma$, $|\sigma_2| = 0.1\gamma$, $\psi_1 = \pi/2$, $\psi_2 = 0.4\pi$.

Figure 26 shows the plots for the real parts of eigenvalues of λ_i, where $i = 1, 2, 3$, versus the mod of Rabi frequency $|\sigma_1|/\gamma$ and phase angle ψ_p at larger and smaller Zeeman width W_z. The real part of three eigenvalues λ_i of a non-Hermitian Hamiltonian is studied at a smaller Zeeman width $W_z = 0.1\gamma$. The real part of eigenvalues shows three second-order exceptional surfaces. The two eigenvalues λ_2 and λ_3 coincide at resonance surface $|\sigma_1| = 16\gamma$, and exceptional surface values are -1000 and $|\sigma_1| = 16\gamma$, showing degeneracy in the range of $16\gamma \leq |\sigma_1| \leq 20\gamma$ and $0 \leq \psi_p \leq 2\pi$. The two eigenvalues λ_2 and λ_3 coincide at resonance surface $|\sigma_1| = 3.9\gamma$ and exceptional surface values are -1000 and $|\sigma_1| = 3.9\gamma$, showing degeneracy in the range of $0 \leq \psi_p \leq 2\pi$. The two eigenvalues λ_1 and λ_3 coincide at resonance surface $|\sigma_1| = 2.9\gamma$, and exceptional surface values are -2000 and $|\sigma_1| = 2.9\gamma$, showing degeneracy in the range of $0\gamma \leq |\sigma_1| \leq 2.9\gamma$ and $0 \leq \psi_p \leq 2\pi$, as illustrated in Figure 26(a). Now, the real part of three eigenvalues λ_i of a non-Hermitian Hamiltonian is studied at a larger Zeeman width $W_z = 10\gamma$. The real part of λ_i shows four second-order exceptional surfaces.The two eigenvalues λ_2 and λ_3 coincide at resonance surface $|\sigma_1| = 13\gamma$, and exceptional surface values are -0.10 and $|\sigma_1| = 13\gamma$, showing degeneracy in the range of $13\gamma \leq |\sigma_1| \leq 20\gamma$ and $0 \leq \psi_p \leq 2\pi$. The two eigenvalues λ_2 and λ_3 coincide at resonance surface $|\sigma_1| = 9.5\gamma$, and exceptional surface values are -0.10 and $|\sigma_1| = 9.5\gamma$, showing degeneracy in the range of $9.5\gamma \leq |\sigma_1| \leq 20\gamma$ and $0 \leq \psi_p \leq 2\pi$. The two eigenvalues λ_2 and λ_3 coincide at resonance surface $|\sigma_1| = 3.9\gamma$, and exceptional surface values are -0.10 and $|\sigma_1| = 3.9\gamma$, showing degeneracy in the range of $0 \leq \psi_p \leq 2\pi$. The two eigenvalues λ_1 and λ_3 coincide at resonance surface $|\sigma_1| = 2.9\gamma$, and exceptional surface values are -0.20 and $|\sigma_1| = 2.9\gamma$, showing degeneracy in the range of $0\gamma \leq |\sigma_1| \leq 2.9\gamma$ and $0 \leq \psi_p \leq 2\pi$, as illustrated in Figure 26(b). The overall results shows that the degeneracy increases with increasing Zeeman width in the real part of eigenvalues.

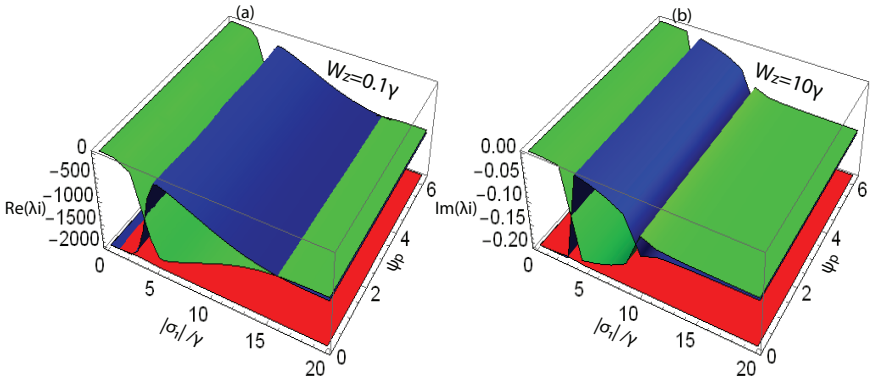

Figure 26. The real part of eigenvalues versus Rabi frequency σ_1 and phase ψ_p. Other parameter values are $\gamma_{21} = 0.9\gamma$, $\gamma_{32} = 0.08\gamma$, $\Delta_1 = -20\gamma$, $\Delta_2 = -20\gamma$, $\Delta_p = 18\gamma$, $|\sigma_p| = 0.1\gamma$, $|\sigma_2| = 0.1\gamma$, $\psi_1 = \pi/2$, $\psi_2 = 0.4\pi$.

3.7. Plots against Zeeman width W_z

Figure 27 displays the real and imaginary parts of eigenvalues of λ_i, where $i = 1, 2, 3$, versus controlled field detuning Δ_1 and Zeeman width W_Z. The imaginary parts of three eigenvalues of non-Hermitian Hamiltonian coincide at the resonance surface $W_Z = 10\gamma$; this is a third-order exceptional surface of non-Hermitian Hamiltonian in a three-level atomic medium, and the exceptional surface values are 0 and $W_Z = 10\gamma$. The three eigenvalues show degeneracy in the range of $10\gamma \leq W_Z \leq 20\gamma$ and $-10\gamma \leq \Delta_p \leq 10\gamma$. The imaginary part of three eigenvalues shows that degeneracy is increases

with increasing Zeeman width, as illustrated in Figure 27. The real parts of three eigenvalues of a non-Hermitian Hamiltonian coincide at the resonance surface $W_Z = 10\gamma$; this is a third-order exceptional surface of a non-Hermitian Hamiltonian in a three-level atomic medium, and the exceptional surface values are 0 and $W_Z = 10\gamma$. The three eigenvalues show degeneracy in the range of $10\gamma \leq W_Z \leq 20\gamma$ and $-10\gamma \leq \Delta_p \leq 10\gamma$. The real part of three eigenvalues shows that degeneracy is increasing with increasing Zeeman width, as illustrated in Figure 27.

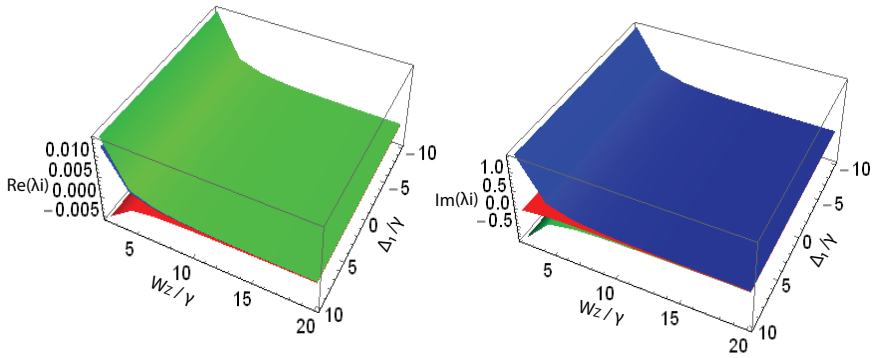

Figure 27. The real and imaginary parts of eigenvalues versus detuning δ_1 and Zeeman width W_z. Other parameter values are $\gamma_{21} = 0.98\gamma$, $\gamma_{32} = 0.98\gamma$, $\Delta_1 = 0.05\gamma$, $\Delta_2 = 0.05\gamma$, $|\sigma_1| = 4\gamma$, $|\sigma_2| = 7\gamma$, $|\sigma_p| = 0.1\gamma$, $\psi_p = 2\pi/2$, $\psi_1 = \pi$, $\psi_2 = \pi/2$.

4. Conclusions

The exceptional surface of a Doppler- and Zeeman-affected non-Hermitian Hamiltonian in a three-level atomic medium is investigated in this manuscript. The eigenvalues and eigenstates of a non-Hermitian Hamiltonian are calculated by using the secular equations $|H - \lambda I| = 0$, and $|H - \lambda I|v = 0$ respectively. The interception of eigenstates and real and imaginary parts of eigenvalues is related to exceptional surfaces. Multiple exceptional surfaces of the second and third orders of non-Hermitian Hamiltonian are reported by real and imaginary parts of the eigenvalues. The exceptional surfaces and degeneracy regions are studied with variations in detuning, control and probe field Rabi frequencies, decay rate, and phases in the absence and presence of the Zeeman effect. The exceptional surfaces are reported to shift with Zeeman and Doppler shifts. The degeneracy increases with an increase in the Zeeman effect. With increase in Doppler width, degeneracy also increases in real part of eigenvalues but decreases in their imaginary part. The maximum range of degeneracy of Zeeman-affected exceptional surfaces is investigated with decay rates and Rabi frequencies of coupled driving fields; Doppler-affected exceptional surfaces are investigated with detuning and Rabi frequencies. The degeneracy of the exceptional surface remains in the range of $0\gamma \leq |\sigma_2| \leq 1.9\gamma$ and $-10\gamma \leq \Delta_p \leq 10\gamma$ on the imaginary part and $5\gamma \leq |\sigma_2| \leq 20\gamma$ and $-10\gamma \leq \Delta_p \leq 10\gamma$ on the real part of eigenvalues in the absence of any shifts. In the presence of Doppler or Zeeman shift, exceptional surfaces shift and changes occur in degeneracy. The modified results of exceptional surfaces are useful for hybrid quantum systems, tactile sensors, artificial intelligence, entanglement physics, optical gyroscopes, thermal mappings, and optics.

Authors Contribution

Abdul Majeed, Obaid J. Algahtani, Imdad Ullah, Amir Ali, and Dragan Pamucar: Conceptualization, Methodology, Validation, Writing-original draft, Writing-review & editing. It is also declared that all the authors have equal contributions to the manuscript. Further, the authors have checked and approved the final version of the manuscript.

Use of Generative-AI tools declaration

The authors declare they have not used Artificial Intelligence (AI) tools in the creation of this article.

Acknowledgments

Ongoing Research Funding Program (ORF-2025-447), King Saud University, Riyadh, Saudi Arabia.

Conflict of interest

It is declared that all authors have no conflict of interest regarding this manuscript.

References

1. M. Berry, M. Wilkinson, Diabolical points in the spectra of triangles, *Proc. R. Soc. Lond. A*, **392** (1984), 15–43. https://doi.org/10.1098/rspa.1984.0022
2. W. Heiss, The physics of exceptional points, *J. Phys. A: Math. Theor.*, **45** (2012), 444016. https://doi.org/10.1088/1751-8113/45/44/444016
3. C. Liang, Y. Tang, A. Xu, Y. Liu, Observation of exceptional points in thermal atomic ensembles, *Phys. Rev. Lett.*, **130** (2023), 263601. https://doi.org/10.1103/PhysRevLett.130.263601
4. I. Ullah, A. Majeed, A. Ali, Z. Khan, Reflection and transmission solitons via high magneto optical medium, *Chaos Soliton. Fract.*, **191** (2025), 115881. https://doi.org/10.1016/j.chaos.2024.115881
5. I. Ullah, A. Majeed, M. Dalam, M. Almazah, A. Ali, Coherent manipulation of tunneling and super Gaussian based Goos-Hänchen shift in five level chiral atomic medium, *Appl. Phys. A*, **131** (2025), 89. https://doi.org/10.1007/s00339-024-08205-z
6. Z. Khan, A. Majeed, I. Ullah, A. Ali, Coherent generation of superluminal and subluminal propagation of structured light in five level atomic medium, *Appl. Phys. B*, **131** (2025), 30. https://doi.org/10.1007/s00340-025-08394-2
7. H. Hodaei, A. Hassan, S. Wittek, H. Garcia-Gracia, R. El-Ganainy, D. Christodoulides, et al., Enhanced sensitivity at higher-order exceptional points, *Nature*, **548** (2017), 187–191. https://doi.org/10.1038/nature23280
8. W. Chen, Ş. Kaya Özdemir, G. Zhao, J. Wiersig, L. Yang, Exceptional points enhance sensing in an optical microcavity, *Nature*, **548** (2017), 192–196. https://doi.org/10.1038/nature23281

9. I. Arkhipov, A. Miranowicz, F. Minganti, F. Nori, Liouvillian exceptional points of any order in dissipative linear bosonic systems: coherence functions and switching between and anti-symmetries, *Phys. Rev. A*, **102** (2020), 033715. https://doi.org/10.1103/PhysRevA.102.033715

10. C. Zheng, Y. An, Z. Wang, X. Qin, B. Eynard, M. Bricogne, et al., Knowledge-based engineering approach for defining robotic manufacturing system architectures, *Int. J. Prod. Res.*, **61** (2023), 1436–1454. https://doi.org/10.1080/00207543.2022.2037025

11. G. Feng, S. Yu, T. Wang, Z. Zhang, Discussion on the weak equivalence principle for a Schwarzschild gravitational field based on the light-clock model, *Ann. Phys.*, **473** (2024), 169903. https://doi.org/10.1016/j.aop.2024.169903

12. R. Thomas, H. Li, F. Ellis, T. Kottos, Giant nonreciprocity near exceptional-point degeneracies, *Phys. Rev. A*, **94** (2016), 043829. https://doi.org/10.1103/PhysRevA.94.043829

13. Z. Wang, Y. Yang, F. Parastesh, S. Cao, J. Wang, Chaotic dynamics of a carbon nanotube oscillator with symmetry-breaking, *Phys. Scr.*, **100** (2025), 015225. https://doi.org/10.1088/1402-4896/ad9552

14. P. Cejnar, J. Jolie, R. Casten, Quantum phase transitions in the shapes of atomic nuclei, *Rev. Mod. Phys.*, **82** (2010), 2155. https://doi.org/10.1103/RevModPhys.82.2155

15. J. Wiersig, Enhancing the sensitivity of frequency and energy splitting detection by using exceptional points: application to microcavity sensors for single-particle detection, *Phys. Rev. Lett.*, **112** (2014), 203901. https://doi.org/10.1103/PhysRevLett.112.203901

16. N. Mortensen, P. Gonçalves, M. Khajavikhan, D. Christodoulides, C. Tserkezis, C. Wolff, Fluctuations and noise-limited sensing near the exceptional point of parity-time-symmetric resonator systems, *Optica*, **5** (2018), 1342–1346. https://doi.org/10.1364/OPTICA.5.001342

17. M. Mohammad-Ali, A. Alu, Exceptional points in optics and photonics, *Science*, **363** (2019), 7709. https://doi.org/10.1126/science.aar7709

18. J. Bouchaud, M. Potters, *Theory of financial risk and derivative pricing: from statistical physics to risk management*, Cambridge: Cambridge University Press, 2003. https://doi.org/10.1017/CBO9780511753893

19. Y. Zhou, X. Wu, X. Cai, H. Xu, Q. Li, W. Xiong, et al., Smart meta-device powered by stray microwave energies: a green approach to shielding external interference and detection, *Appl. Energ.*, **378** (2025), 124770. https://doi.org/10.1016/j.apenergy.2024.124770

20. Y. Lai, Y. Lu, M. Suh, K. Vahala, Enhanced sensitivity operation of an optical gyroscope near an exceptional point, *Nature*, **576** (2019), 65–69. https://doi.org/10.1038/s41586-019-1777-z

21. H. Jing, Ş. Özdemir, H. Lü, F. Nori, High-order exceptional points in optomechanics, *Sci. Rep.*, **7** (2017), 3386. https://doi.org/10.1038/s41598-017-03546-7

22. H. Zhao, Z. Chen, R. Zhao, L. Feng, Exceptional point engineered glass slide for microscopic thermal mapping, *Nat. Commun.*, **9** (2018), 1764. https://doi.org/10.1038/s41467-018-04251-3

23. W. Sun, Y. Jin, G. Lu, Genuine multipartite entanglement from a thermodynamic perspective, *Phys. Rev. A*, **109** (2024), 042422. https://doi.org/10.1103/PhysRevA.109.042422

24. S. Abo, P. Tulewicz, K. Bartkiewicz, Ş. Özdemir, A. Miranowicz, Experimental Liouvillian exceptional points in a quantum system without Hamiltonian singularities, *New J. Phys.*, **26** (2024), 123032. https://doi.org/10.1088/1367-2630/ad98b6
25. C. Shi, D. Wang, W. Li, X. Fang, B. Zhang, D. Wang, Atomic imaging and optical properties of InAs/In0.5Ga0.5As0.5Sb0.5 type II superlattice, *Appl. Phys. Lett.*, **124** (2024), 251101. https://doi.org/10.1063/5.0209805
26. A. Lakhtakia, T. Mackay, C. Zhou, Electromagnetic surface waves at exceptional points, *Eur. J. Phys.*, **42** (2020), 015302. https://doi.org/10.1088/1361-6404/abb6c7
27. M. Scheffer, J. Bascompte, W. Brock, V. Brovkin, S. Carpenter, V. Dakos, et al., Early-warning signals for critical transitions, *Nature*, **461** (2009), 53–59. https://doi.org/10.1038/nature08227
28. Ş. Özdemir, S. Rotter, F. Nori, L. Yang, Parity-time symmetry and exceptional points in photonics, *Nat. Mater.*, **18** (2019), 783–798. https://doi.org/10.1038/s41563-019-0304-9
29. Y. Wu, P. Zhou, T. Li, W. Wan, Y. Zou, High-order exceptional point based optical sensor, *Opt. Express*, **29** (2021), 6080–6091. https://doi.org/10.1364/OE.418644
30. R. Duggan, S. Mann, A. Alù, Limitations of sensing at an exceptional point, *ACS Photonics*, **9** (2022), 1554–1566. https://doi.org/10.1021/acsphotonics.1c01535
31. G. Zhang, Z. Chen, D. Xu, N. Shammah, M. Liao, T. Li, et al., Exceptional point and cross-relaxation effect in a hybrid quantum system, *PRX Quantum*, **2** (2021), 020307. https://doi.org/10.1103/PRXQuantum.2.020307
32. T. Goldzak, A. Mailybaev, N. Moiseyev, Light stops at exceptional points, *Phys. Rev. Lett.*, **120** (2018), 013901. https://doi.org/10.1103/PhysRevLett.120.013901
33. I. Mandal, E. Bergholtz, Symmetry and higher-order exceptional points, *Phys. Rev. Lett.*, **127** (2021), 186601. https://doi.org/10.1103/PhysRevLett.127.186601
34. X. Zhang, C. Chan, Dynamically encircling exceptional points in a three-mod waveguide system, *Commun. Phys.*, **2** (2019), 63. https://doi.org/10.1038/s42005-019-0171-3
35. K. Kawabata, Exceptional sensing and transport, *Physics*, **16** (2023), 107. https://doi.org/10.1103/Physics.16.107
36. S. Ramezanpour, A. Bogdanov, Tuning exceptional points with Kerr nonlinearity, *Phys. Rev. A*, **103** (2021), 043510. https://doi.org/10.1103/PhysRevA.103.043510
37. M. Brandstetter, M. Liertzer, C. Deutsch, P. Klang, J. Schöberl, H. Türeci, et al., Reversing the pump dependence of a laser at an exceptional point, *Nat. Commun.*, **5** (2014), 4034. https://doi.org/10.1038/ncomms5034
38. A. Kodigala, T. Lepetit, B. Kanté, Exceptional points in three-dimensional plasmonic nanostructures, *Phys. Rev. B*, **94** (2016), 201103(R). https://doi.org/10.1103/PhysRevB.94.201103
39. H. Chen, T. Liu, H. Luan, R. Liu, X. Wang, X. Zhu, et al., Revealing the missing dimension at an exceptional point, *Nat. Phys.*, **16** (2020), 571–578. https://doi.org/10.1038/s41567-020-0807-y
40. J. Zhang, B. Peng, Ş. Özdemir, K. Pichler, D. Krimer, G. Zhao, et al., A phonon laser operating at an exceptional point, *Nature Photon.*, **12** (2018), 479–484. https://doi.org/10.1038/s41566-018-0213-5

41. C. Wolff, C. Tserkezis, N. Mortensen, On the time evolution at a fluctuating exceptional point, *Nanophotonics*, **8** (2019), 1319–1326. https://doi.org/10.1515/nanoph-2019-0036

42. N. Even, B. Nennig, G. Lefebvre, E. Perrey-Debain, Experimental observation of exceptional points in coupled pendulums, *J. Sound Vib.*, **575** (2024), 118239. https://doi.org/10.1016/j.jsv.2024.118239

43. E. Bulgakov, K. Pichugin, A. Sadreev, Exceptional points in a dielectric spheroid, *Phys. Rev. A*, **104** (2021), 053507. https://doi.org/10.1103/PhysRevA.104.053507

44. H. Iqbal, M. Idrees, M. Javed, B. Bacha, S. Khan, S. Ullah, Goos-Hänchen shift from cold and hot atomic media using Kerr nonlinearity, *J. Russ. Laser Res.*, **38** (2017), 426–436. https://doi.org/10.1007/s10946-017-9663-3

45. K. Ding, G. Ma, M. Xiao, Z. Zhang, C. Chan, Emergence, coalescence, and topological properties of multiple exceptional points and their experimental realization, *Phys. Rev. X*, **6** (2016), 021007. https://doi.org/10.1103/PhysRevX.6.021007

AIMS Press